

MASSIVE STARS IN THE RANGE $13 - 25 M_{\odot}$: EVOLUTION AND NUCLEOSYNTHESIS. II. THE SOLAR METALLICITY MODELS.

Marco Limongi¹, Oscar Straniero² and Alessandro Chieffi^{1,3}

1. Osservatorio Astronomico di Roma, Via Frascati 33, I-00040, Monteporzio Catone, Italy;
marco@nemo.mporzio.astro.it
2. Osservatorio Astronomico di Collurania, I-64100, Teramo, Italy;
straniero@astrte.te.astro.it
3. Istituto di Astrofisica Spaziale (CNR), Via Fosso del Cavaliere, I-00133, Roma, Italy;
achieffi@ias.rm.cnr.it

Received _____; accepted _____

To be submitted to the Astrophysical Journal

ABSTRACT

We present the evolutionary properties of a set of massive stellar models (namely 13, 15, 20 and 25 M_{\odot}) from the main sequence phase up to the onset of the iron core collapse. All these models have initial solar chemical composition, i.e. $Y = 0.285$ and $Z = 0.02$. A 179 isotope network, extending from neutron up to ^{68}Zn and fully coupled to the evolutionary code has been adopted from the Carbon burning onward. Our results are compared, whenever possible, to similar computations available in literature.

Subject headings: nuclear reactions, nucleosynthesis, abundances – stars: evolution – stars: interiors – stars: supernovae

1. Introduction

This is the second paper in a series devoted to a detailed study of the evolutionary properties of massive stars up to the onset of the final collapse. In the first paper of this series ((3) 1998 - hereinafter Paper I) we have discussed in some detail the relevant literature on the subject and the improvements progressively made in the computation of the advanced burning phases in these last two decades: such a discussion will not be repeated here. We discussed also the latest version of our evolutionary code FRANEC (version 4.2) together with the evolutionary properties of a 25 M_{\odot} star, from the Pre Main Sequence up to the onset of the collapse. That evolution was computed by adopting a network which included 12 isotopes for the H burning, 25 isotopes for the He burning and 149 isotopes for all the more advanced burning phases. Though such a network was well suited to present that first test model, an accurate tracing of the chemical evolution of the matter requires a significantly larger nuclear network and hence we now adopt in all our computations a much

more extended network (see section 2) with respect to the one adopted in Paper I.

In this paper we present the hydrostatic evolution of a first set of massive stars in the mass range $13 - 25 M_{\odot}$ while in the next one of the series we will present the evolution of metal poor ($Z = 10^{-3}$ and $Z = 0$) massive stars together with the explosive yields. For the moment we did not extend the computations outside of this mass range because a) stars less massive than $13 M_{\odot}$ are close enough to the limit of semidegenerate C ignition that the computer time required to follow them becomes exceedingly large for the computers we have at present and b) stars more massive than $25 M_{\odot}$ begin to be significantly affected by mass loss, phenomenon which we do not want to include yet.

Each subsection of section 3 will be devoted to the analysis of a specific burning (both central and in shell) and to its dependence on the initial mass. Section 4 is devoted to a general discussion of the results together with a comparison with similar computations available in literature.

A last summary and conclusions follows.

Since at the end of the writing of this paper the computation of all the other masses of lower metallicity (i.e. $Z = 0$ and $Z = 10^{-3}$) were completed together with their explosive nucleosynthesis, since our tables of explosive yields have been already distributed to many researchers, and since at present they are also available at the web site

<http://www.mporzio.astro.it/~mandrake/orfeo.html>

we decided to add our full set of the elemental explosive yields as appendix A to the present paper.

2. Numerical methods and input physics

All the models have been computed by means of the evolutionary code FRANEC (ver. 4.2) whose earliest and latest versions have been presented in (Chieffi and Straniero) (1989) and Paper I respectively. The main properties of the code are the following. The nuclear network includes 41 isotopes for the H burning, 88 isotopes for the He burning and 179 isotopes for the more advanced phases; a list of the isotopes adopted in these three regimes is shown in Table 1.

EDITOR: PLACE TABLE 1 HERE.

The extension of the convective regions are fixed by means of the Schwarzschild criterion, and no mechanical overshooting is allowed. On the contrary the semiconvection and the induced overshooting, due to the transformation of He in C and O during core helium burning, are properly taken into account following (Castellani et al.) (1985). During the last phases of central He burning the breathing pulses have been inhibited as described in (Caputo et al.) (1989) and in (Chieffi and Straniero) (1989). In the convective layers superadiabaticity was taken into account following the derivation of (Cox and Giuli) (1968) of the mixing-length formalism of Böhm-Vitense.

The nuclear reaction rates are taken from the database kindly provided by Thielemann (private communication). For the $^{12}\text{C}(\alpha, \gamma)^{16}\text{O}$ reaction we adopted the old value from (Caughlan et al.) (1985). The weak interaction rates as a function of the temperature and density were taken from (5) (1980), (6) (1982) and (7) (1985). For the nuclei not included in this database, terrestrial half-lives have been adopted. The electron screenings are taken from (Graboske et al.) (1973) and (4) (1973) for the weak, intermediate and intermediate-strong regime, and from (9) (1977) and (Itoh et al.) (1979) for the strong regime.

The equation of state (EOS) is the one described by (Straniero) (1988) and updated by (13) (1997).

The radiative opacity coefficients are derived from (Kurucz) (1991), (8) (1992) (OPAL) and from the Los Alamos Opacity Library (LAOL) ((Huebner et al.) 1977). The heavy element solar mixture by (Grevesse) (1991) has been adopted. The opacity coefficients due to the thermal conductivity are derived from (Itoh et al.) (1983).

The energy loss due to photo, pair and plasma neutrinos are properly taken into account following (11) (1985) (corrected as reported by (12) 1986). Bremsstrahlung neutrinos are taken into account following (Dicus et al.) (1976) (corrected by (Richardson et al.) 1982) who extended the results obtained by (Festa and Rudermann) (1969) by the inclusion of the neutral current effects. The energy loss due to the recombination processes are included following the prescriptions of (2) (1967).

No mass loss has been included in the calculations.

3. Evolutionary results

We followed the evolution of four stellar models of 13, 15, 20 and 25 M_{\odot} , having an initial solar chemical composition (i.e. $Z = 0.02$ and $Y = 0.285$), from the pre main sequence phase up to the onset of the iron core collapse. As usual the initial He abundance and the value for the mixing length parameter ($\alpha = l/H_P$) have been fixed by fitting the present properties of the Sun (see (13) 1997). The pre main sequence evolution has been followed by assuming the star to settle on the Hayashi track directly with its final main sequence mass.

The main evolutionary properties of all the computed models up to the precollapse stage (referred to, in the following, as the "final" model) are summarized in Table 2.

EDITOR: PLACE TABLE 2 HERE.

The path followed by the star models in both the HR and the $\text{Log}T_c$ - $\text{Log}\rho_c$ diagrams are shown in Figures 1 and 2, while

EDITOR: PLACE FIGURE 1 HERE.

EDITOR: PLACE FIGURE 2 HERE.

the evolution of the convective zones from the MS up to the central C ignition is shown in Figure 3;

EDITOR: PLACE FIGURE 3 HERE.

Figure 4 shows the temporal evolution of the radius of the internal mass layers (in steps of $1 M_\odot$) from the central H exhaustion up to the presupernova stage.

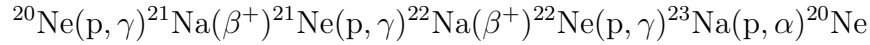
EDITOR: PLACE FIGURE 4 HERE.

3.1. H burning

The key properties of the four star models during central H burning are reported in Table 2 (section "H burning") from column (2) to column (5). The various quantities in column (1) refer to: the H burning lifetime in years (τ_H); the maximum extension of the H convective core in solar masses (M_{cc}); the time duration of the H convective shell in years ($\Delta t_{H \text{ conv shell}}$); the maximum extension of the H convective shell in solar masses ($\Delta M_{H \text{ conv shell}}$); the final location of the H burning shell (defined as the mass coordinate corresponding to the maximum

of the nuclear energy generation rate provided by the H burning reactions) in solar masses ($M_{H\text{ shell}}^{\text{final}}$); the final location of the He core (defined as the mass location corresponding to the H/He interface) in solar masses ($M_{\text{He core}}^{\text{final}}$); the final location of both the H burning shell and the He core in solar radii (respectively $R_{H\text{ shell}}^{\text{final}}$ and $R_{\text{He core}}^{\text{final}}$).

Central H burning proceeds, as it is well known, through the CNO cycle. The central temperature is high enough (between $\log T = 7.5$ and $\log T = 7.8$) for both the Ne-Na and the Mg-Al cycles to become efficient:



As a consequence, at the end of H burning, ^{21}Ne and ^{25}Mg are almost completely destroyed, ^{22}Ne is reduced by almost an order of magnitude, ^{23}Na and ^{26}Mg increase by a factor of ~ 6 and ~ 2 respectively, ^{26}Al increases to a mass fraction of $\sim 10^{-6}$ for the $13 M_{\odot}$ and $\sim 10^{-7}$ for all the others, while ^{20}Ne , ^{24}Mg and ^{27}Al remain almost unaltered. The central abundances of all these isotopes at the end of the H burning phase (specifically when the H mass fraction reduces to 10^{-3}) are reported in Table 3 (section "H burning") for all the four models (columns 2 to 5).

EDITOR: PLACE TABLE 3 HERE.

All models form an H convective shell just before the central H exhaustion. How it is well known (see e.g. (10) 1989), the efficiency of the mixing in this region determines if the star will ignite the He at the blue side or at the red side of the Hertzsprung gap: since we chose arbitrarily to adopt the Schwarzschild criterion, all our models ignite He at the blue (quite obviously, the inclusion of mass loss in the computation of these stars could in principle alter,

even significantly, the path followed by the star in the HR diagram). The further behavior of the surface properties of all the models depends on the mass (see Figures 3, 4 and 5).

EDITOR: PLACE FIGURE 5 HERE.

In the two lower mass models the H convective shell vanishes rather soon and hence the models early move towards the Hayashi track where most of the central He burning occurs. The two more massive models show, on the contrary, a stable H convective shell which lasts for all the central He burning lifetime and hence they remain at the blue side of the Hertzsprung gap up to almost the end of the central He burning phase.

As each star approaches its Hayashi track, a convective envelope appears and penetrates inward in mass. When the convective envelope reaches the mass location marking the maximum extension attained by the H convective shell, it begins to dredge up material modified by the H burning to the surface. Since both the 20 and 25 M_{\odot} models form a long lasting convective H burning shell which largely overlaps part of the previous convective core, the matter dredged up to the surface experiences two successive H burning episodes. On the contrary the matter dredged up to the surface by both the 13 M_{\odot} and the 15 M_{\odot} was modified only by the central H burning since in this case the H convective shell did not last enough to induce a sizeable modification in the chemical composition.

The convective envelope reaches its maximum depth just before the central neon ignition in all the four models; at this point the residual time before the explosion is $\simeq 145$ yr for the 13 M_{\odot} , $\simeq 85$ yr for the 15 M_{\odot} , $\simeq 77$ yr for the 20 M_{\odot} , and $\simeq 63$ yr for the 25 M_{\odot} . During this residual time the surface chemical composition remains practically frozen due to the more rapid evolution of the core compared to that of the envelope. Section "Convective Envelope" in Table 2 reports, for all the four models, (column 2 to 5) the final locations of the inner boundary of the convective envelope in solar masses ($M_{\text{conv. env}}^{\text{final}}$) and the final surface

isotopic ratios $^{12}\text{C}/^{13}\text{C}$, $^{14}\text{N}/^{15}\text{N}$, $^{16}\text{O}/^{17}\text{O}$ and $^{16}\text{O}/^{18}\text{O}$. The final surface abundances in mass fraction for all the nuclear species modified by the H burning are reported in Table 4 for all the four models (columns 3 to 6) compared to the solar values (column 2). Note that in both the 20 and 25 M_\odot models the convective H burning shell contributes to the final surface abundance of several species, i.e. ^{16}O , ^{17}O , ^{23}Na , ^{26}Mg , ^{21}Ne , ^{25}Mg and ^{26}Al : this last isotope in particular is almost completely produced by the convective H burning shell.

EDITOR: PLACE TABLE 4 HERE.

The temporal behavior of both the mass and radius of the H burning shell (defined as the mass corresponding to the maximum energy generation rate of the H burning) is shown in Figure 6 as a function of the central temperature up to the moment of the explosion.

EDITOR: PLACE FIGURE 6 HERE.

The burning front advances in mass up to the end of the central He burning phase and then it switches off completely when the formation of an efficient He burning shell induces a robust expansion and hence the cooling of the H rich layers: note that the final radius of the H shell scales inversely with the total mass, i.e., the larger the initial mass the smaller the final H shell radius (see section 4).

As a final comment on the behavior of the envelope, let us remark that the Kelvin Helmholtz timescale for the envelope ($t_{KH} \simeq 2 \cdot 10^7 M_{\text{core}} M_{\text{envelope}} / RL_{\text{sup}}$), i.e. the timescale necessary to move (in the HR diagram) from the red to the blue, and/or vice versa, is for all the four masses of the order of 15 ± 5 yr. This means that (at least in the case of no mass loss) the position of all these stars in the HR diagram can vary in principle up to ~ 15 yr before the explosion.

3.2. He burning

The main properties of the central He burning for the four stellar models are reported in Table 2 (section "He burning"). The various quantities in column (1) are: the time delay between the central H exhaustion and the central He ignition in years ($\Delta t(\text{H exh.} - \text{He ign.})$); the He burning lifetime in years (τ_{He}); the maximum extension of the He convective core in solar masses (M_{cc}); the central ^{12}C and ^{16}O mass fractions left by the central He burning; the time duration in years and the maximum extension in solar masses of the first and the second He convective shells (respectively $\Delta t_{1 \text{ He conv shell}}$, $\Delta M_{1 \text{ He conv shell}}$, $\Delta t_{2 \text{ He conv shell}}$ and $\Delta M_{2 \text{ He conv shell}}$); the final location of the He burning shell (defined as the mass coordinate corresponding to the maximum of the nuclear energy generation rate provided by the He burning reactions) in solar masses ($M_{\text{He shell}}^{\text{final}}$); the final location of the CO core (namely the He exhausted core) in solar masses ($M_{\text{CO core}}^{\text{final}}$); the final locations of both the He burning shell and the CO core in solar radii (respectively $R_{\text{He shell}}^{\text{final}}$ and $R_{\text{CO core}}^{\text{final}}$).

This phase is characterized by the presence of a convective core which advances progressively in mass during all the central burning (see figure 3) and by the conversion firstly of He into ^{12}C and then of ^{12}C into ^{16}O via the $^{12}\text{C}(\alpha, \gamma)^{16}\text{O}$ reaction. In addition to that, ^{14}N (which roughly equates the sum of the initial abundances of the nuclear species previously involved in the CNO cycle) is completely converted into ^{22}Ne which, in turn, is partially destroyed by the neutron producing reaction $^{22}\text{Ne}(\alpha, n)^{25}\text{Mg}$.

At variance with the He core mass, whose final value is determined by both the size of the convective core in the H burning phase and by the advancing of the H shell in the following central He burning phase, the final value of the CO core mass is determined only by the size of the convective core at the end of the central He burning; the further evolutionary phases, in fact, are fast enough that the main He convective shell which forms just outside the previous border of the convective core does not have time enough to burn the available fuel

and hence to further advance in mass. This means that the abundances of ^{12}C and ^{16}O within the whole CO core are essentially flat and fixed by the (convective) central He burning phase and not by a shell (radiative or convective) burning. As it has been recognized a long time ago (see e.g. (Arnett) 1972, (Thielemann and Arnett) 1985, (Woosley and Weaver) 1986 and (Weaver and Woosley) 1993) the amount of carbon left by the central He burning phase strongly influences the further evolutionary phases because it determines the amount of fuel available for both the central and shell C burning (see next section). It is important to stress here that the final amount of Carbon left by the central He burning depends on the efficiency of the $^{12}\text{C}(\alpha, \gamma)^{16}\text{O}$ reaction rate which, in turn, depends on both the amount of available fuel (mainly He) and the nuclear cross section of the process: in particular, either a larger nuclear cross section or a larger convective core tend to lower the final carbon abundance. This means that the same final abundance of ^{12}C may be obtained by adopting a proper combination of different choices for both the size of the convective core and the nuclear cross section. It is worthful to underline that both the extension of the convective core and the $^{12}\text{C}(\alpha, \gamma)^{16}\text{O}$ cross section are still affected by large uncertainties. It goes without saying that this degeneracy between convection and nuclear cross section will be removed as soon as the ongoing experiments devoted to new measures of the nuclear cross section closer to the Gamow peak will be completed.

A further difficulty is connected with the possible presence of the so called Breathing Pulses. These instabilities occur during the last part of the central He burning (typically when the central He mass fraction drops below 0.1) and their effect is to induce an extra mixing which brings new fuel in the convective core. It exists a longstanding debate about the real existence of this phenomenon (see (Caputo et al.) 1989 and (Chieffi and Straniero) 1989 for a comprehensive discussion on this subject) which we do not want to address in this paper. We want simply to remark here that the inclusion or the damping of these "Breathing Pulses" will significantly alter the final carbon abundance.

For the moment, and for sake of clearness, let us clearly repeat that the results shown in Table 2 have been obtained in the following scheme: 1) $^{12}\text{C}(\alpha, \gamma)^{16}\text{O}$ rate by (Caughlan et al.) (1985), 2) Schwarzschild criterion (to check for convective instabilities), 3) inclusion of both the "induced" overshooting and semiconvection (see (Castellani et al.) 1985), 4) inhibition of the Breathing Pulses if they occur.

As a final comment on the central He burning, let us note that while the final CO core scales directly with the mass, i.e. the larger the mass the larger the final CO core, the $^{12}\text{C}/^{16}\text{O}$ ratio at the end of central He burning remains almost flat in the mass range 15 to 25 M_\odot while it increases significantly in the 13 M_\odot .

Once the He is exhausted at the center, the burning shifts outer in mass and locates at the He discontinuity left by the convective core. The following evolution of the He burning is characterized in all four cases by the formation of two successive, and overlapping, convective shells episodes: the first one extends over a small mass range while the second one, which will last up to the collapse, extends on a much larger zone. In particular the mass size of this second convective He shell is mainly confined between the He discontinuity left by the convective core (i.e. the outer edge of the CO core) and the He core mass. Since the He core mass grows with the initial mass more rapidly than the CO core mass, the mass size of the He convective shell increases with the initial mass of the star (see Table 2). The final and typical chemical composition present in the He convective shell is obviously largely dominated by He (more than 0.8 by mass fraction) and by carbon and oxygen. In the three more massive models the carbon abundance in the convective shell is almost twice the oxygen one while in the smaller mass the oxygen abundance is similar to the carbon one: this is due to the occurrence that in the 13 M_\odot the internal border of the convective shell moves inward enough to bring part of the oxygen left by the previous central He burning within the convective shell. ^{14}N is fully converted into ^{22}Ne while only a marginal fraction of it is

converted in ^{25}Mg . All the main data concerning this phase are reported in Table 2.

As a final remark let us note that, contrarily to the behavior of the H shell, the final radius of the He shell scales directly with the initial mass (see Table 2).

3.3. The advanced evolutionary phases

The CO core left by the central He burning speeds up its contraction in order to gain from the gravitational field the energy that the nuclear processes are not able to provide any more. During this phase the core of these massive stars enters a region of the $\rho - T$ plane in which neutrino emission (essentially pair production) becomes very efficient: such strong neutrino emission will continuously increase all along the further evolutionary phases up to the final collapse. The importance of the neutrino losses has been recognized long time ago (see, e.g., (15) 1972 and (Woosley and Weaver) 1986) and in fact the advanced evolutionary phases have always been regarded as "neutrino dominated". Figure 7 shows the temporal behavior (for each mass) of the surface luminosity (energy lost by photons - dashed line), of the neutrino luminosity (energy lost by neutrinos - dotted line) and of the nuclear luminosity (energy produced by all nuclear processes within the stars - solid line).

EDITOR: PLACE FIGURE 7 HERE.

A comparison between the photon and neutrino luminosities clearly shows that the main energy losses occur from the surface of the star up to the carbon ignition (see label C in Figure 7) and from the center in the more advanced burnings; since the nuclear luminosity is regulated by the energy losses (it simply refurnishes the star of the energy lost) it is clear that it closely follows the photon luminosity first and the neutrino luminosity later. In the 20 and $25 M_{\odot}$ stellar models the nuclear energy during the advanced phases (after point C in Figure 7) is not able to produce enough energy to fully sustain the star (the solid line runs

below the dotted one) until the central Ne ignition: in these cases the contraction speeds up in order to gain the missing energy from the gravitational field. The various peaks which are visible in the nuclear luminosity mark the formation of convective episodes (core or shell).

Let us now turn to a more specific analysis of the various burning phases as a function of the initial mass of the star.

3.4. C burning

Carbon burning occurs few 10^4 yr after the central He exhaustion. This evolutionary phase totally depends on the amount of carbon left by the central He burning since it fixes the amount of available fuel. Moreover, since the neutrinos begin to be a major source of energy loss from the center of the star, also the formation of a convective core strictly depends on the initial carbon abundance: in fact the minimum necessary (but not sufficient) requirement to form a convective core is the existence of a positive flux, which implies that the nuclear energy generation rate must exceed the neutrino losses; since the nuclear energy generation rate directly scales with the amount of fuel, it is clear that a larger initial carbon abundance favors the formation of a convective core.

As we have already noted in section 3.2, three out of the four models (15, 20 and 25) have a very similar central carbon abundance at the end of central He burning; in spite of this similarity the $15 M_\odot$ develops a convective core which is not present in the other two more massive models (see Figure 8).

EDITOR: PLACE FIGURE 8 HERE.

The reason was already pointed out by (Arnett) (1972) and, later on, by (Woosley and Weaver) (1986) and is that the neutrino losses (pair production) scale inversely with the density while

the nuclear energy production scales directly with the density. Since the larger the CO core the lower the density (at each given temperature), the balance between gains and losses becomes progressively more negative as the CO mass increases. As an example figure 9 shows a comparison between the $15 M_{\odot}$ (solid line) and the $25 M_{\odot}$ (dashed line).

EDITOR: PLACE FIGURE 9 HERE.

Panels a) and b) in Figure 9 show, respectively, the run of the central carbon abundance and of the density versus the central temperature, while panels c) and d) show, respectively, the central run of the nuclear and the neutrinos energy generation rates. The vertical short dashed line marks the temperature at which the convective core begins to develop in the $15 M_{\odot}$. A comparison between panels c) and d) clearly demonstrates that the balance between nuclear and neutrinos energy generation rates is negative for the more massive star and positive for the smaller one: hence only the smaller of the two masses fulfill the basic requirement for the formation of a convective core.

The main properties of the stellar models related to the C burning are reported in Table 2 in section "C burning". The nuclear processes active in this phase are roughly the same already discussed in Paper I though the final most abundant nuclear species (see Table 3) differ from one model to the other because of the different conditions in which carbon burning occurs (i.e. temperature, density, convective core, etc.). As the interplay between the local nuclear burning and the convective mixing is concerned, we find that the typical mixing turnover time within the convective core is of the order of 10^{-3} yr in both the less massive models, i.e. small enough to allow almost all the nuclear species to be homogeneously mixed.

Similarly to the previous evolutionary phases, once the carbon is exhausted in the center, a burning shell forms which begins to move forward in mass. Figure 10 shows the location of the C burning shell (solid line) superimposed to the convective zones as a function of time.

The behavior of this burning front and hence its final location depends on the interplay among many factors, the main ones being the amount of fuel which is encountered on the way out, the possible formation of convective shells and the time available to the burning front to move further out. In our computations the C burning shell advances in mass essentially until the central silicon ignition because at this point the time left before the explosion is so short (see Table 2) that the C burning shell cannot significantly advance in mass any more. The mass size between the outer border of the last C convective shell and the He shell is negligible in the $13 M_{\odot}$ case while it progressively increases up to $0.6 M_{\odot}$ for the $25 M_{\odot}$; this means that while in the smaller masses essentially no layer exposed to just the central He burning is preserved, for the larger masses a progressively larger layer of material subject to only the central He burning (and hence the C/O ratio) is preserved up to the final explosion.

EDITOR: PLACE FIGURE 10 HERE.

Since the temporal behavior of the carbon convective shells may have important consequences for the s-process nucleosynthesis, we report in Tables 5 and 6 some selected properties of the bottom of the carbon convective shells for two models, i.e. the $15 M_{\odot}$ and the $25 M_{\odot}$, before and after each convective episode (four for the $15 M_{\odot}$ and two for the $25 M_{\odot}$).

EDITOR: PLACE TABLE 5 HERE.

EDITOR: PLACE TABLE 6 HERE.

During shell C burning, the most efficient neutron producer is the $^{22}\text{Ne}(\alpha, n)^{25}\text{Mg}$ reaction which is almost always of the order of $\sim 10\%$ of the maximum integrated flux. By the way let

us remind that the integrated flux of a nuclear process is defined as the integral of its reaction rate over a given time interval. Note that in Tables 5 and 6 the reaction having the maximum integrated flux (i.e., the most efficient one) changes as a function of the mass. The most efficient neutron poisons are basically the $^{25}\text{Mg}(\text{n}, \gamma)^{26}\text{Mg}$, $^{24}\text{Mg}(\text{n}, \gamma)^{25}\text{Mg}$, $^{23}\text{Na}(\text{n}, \gamma)^{24}\text{Na}$ and $^{27}\text{Al}(\text{n}, \gamma)^{28}\text{Al}$ reactions, whose relative and absolute efficiencies vary from one model to the other and during the various convective episodes. Note that the process $^{20}\text{Ne}(\text{n}, \gamma)^{21}\text{Ne}$, though it is very efficient, cannot be considered as a neutron poison, but at most as a modulator of the neutron flux, since it is immediately followed by the $^{21}\text{Ne}(\alpha, \text{n})^{24}\text{Mg}$ which reemits the previously absorbed neutron. Within each convective shell ^{12}C and ^{22}Ne are partially destroyed while the abundances of ^{20}Ne , ^{23}Na , ^{24}Mg , ^{25}Mg and ^{27}Al are slightly increased by an amount which varies from one model to the other and depending on the convective episode. The temperature and density at the bottom of the convective shell vary between $7.8 \cdot 10^8$ K and $3.3 \cdot 10^5$ gm/cm³ (the first convective episode of the $15 M_\odot$ model) and $1.4 \cdot 10^9$ K and $1.14 \cdot 10^5$ gm/cm³ (the last convective shell of the $25 M_\odot$ model). Note that the temperature increases while the density decreases from a convective episode to the following one, the temperature being larger and the density being lower with increasing the mass of the star. For each model the maximum neutron density (number of free electron per unit volume) increases from a convective shell to the following one; during each convective episode, for each mass coordinate, it fastly increases to its maximum value and then it lowers following an almost exponential law.

The final location in mass and radius of the carbon burning shell, in all the computed models, is reported in Table 2.

3.5. Ne burning

As the central temperature reaches $\simeq 1.3 \cdot 10^9$ K Ne burning takes place. The time which elapses between the end of the central carbon burning and the onset of the Ne burning ranges between 1500 yr (for the $13 M_{\odot}$) and 92 yr (for the $25 M_{\odot}$). At this stage the carbon burning shell is located, for the four models, at $1.40 M_{\odot}$ ($13 M_{\odot}$), $1.48 M_{\odot}$ ($15 M_{\odot}$), $1.46 M_{\odot}$ ($20 M_{\odot}$) and $1.51 M_{\odot}$ ($25 M_{\odot}$) and the number of convective C shell episodes already experienced up to this moment are: three ($13 M_{\odot}$ and $15 M_{\odot}$), two ($20 M_{\odot}$) and one ($25 M_{\odot}$) (see Figures 8 and 10). Neon burning occurs in a convective core in all the four models since the amount of available fuel is always sufficient for the nuclear energy production to overcome the neutrino losses. The neon abundance almost equates the preexisting carbon abundance (by number) since it is its main product and hence it directly depends on the choices made for the He burning (see section 3.2).

The main properties of the central neon burning for all the computed models are reported in Table 2, while the main nuclear species left at the end of the central neon burning (i.e. the ones whose mass fraction is greater than 0.01) are reported in Table 3. The dominant processes involved in this burning have also been discussed in Paper I and will not be repeated here.

As the central neon mass fraction drops below $\sim 10^{-4}$ the neon burning shifts in a shell. The following evolution of the burning front strictly follows the fate of the inner core in the sense that it almost stops its advancing during the main burnings (central and shell oxygen burnings and central silicon burning) while it significantly advances in mass between two consecutive burnings. The reason is that the "ensemble" of all the more advanced burnings lasts so short that the neon shell does not have time to advance: only between two successive burnings the cores experience a strong contraction and heating which induces a sudden burning (and hence advancing) of the Ne shell. The situation is discussed in detail

in Paper I and occurs in the same way in all the models presented here.

A neon convective shell forms only in the $15 M_{\odot}$ just after the central oxygen exhaustion; it is located at a mass coordinate of $0.93 M_{\odot}$ and reaches its maximum extension between 0.93 and $1.24 M_{\odot}$ in $\simeq 0.05$ yr when the local ^{20}Ne mass fraction is reduced to $\sim 10^{-4}$ and then it recedes in mass.

The final location in mass and radius of the neon burning shell is reported in Table 2.

3.6. O burning

Central oxygen burning starts just after the central neon exhaustion. It always occurs in a convective core since the nuclear energy production is always large enough to overcome the neutrino losses. At variance with the previous central burnings, the size of the convective core does not depend significantly on the mass but it is always of the order of $1 M_{\odot}$ (see Table 2). The central O burning lifetime ranges between 8 yr for the $13 M_{\odot}$ and 0.33 yr for the $25 M_{\odot}$. The timescale of this burning is short enough that all the various burning shells (Ne, C, He and H) remain practically freezed out during this phase. Since the more advanced evolutionary phases are even faster, the various shells (apart from the Ne one) will remain freezed out up to the moment of the final collapse. The Ne shell, as already addressed in the previous section, is the only exception because it is located in a zone which undergoes a strong contraction and heating after the central oxygen burning and hence it is the only one which may significantly advance in mass anyway.

The most efficient nuclear processes are fairly the same already discussed in Paper I even if the final nucleosynthesis (Table 3) depends appreciably on the initial mass. In particular it happens that while ^{28}Si , ^{32}S and ^{38}Ar are the most abundant nuclei in the two more massive models, in the two less massive ones the two most abundant nuclei, other than

^{28}Si , become ^{30}Si and ^{34}S , i.e. more neutron rich nuclei. This is due to the well known occurrence that during central oxygen burning many weak processes become efficient (in particular the processes $^{31}\text{S}(\beta^+)^{31}\text{P}$, $^{33}\text{S}(\text{e}^-, \nu)^{33}\text{P}$, $^{30}\text{P}(\text{e}^-, \nu)^{30}\text{Si}$ and $^{37}\text{Ar}(\text{e}^-, \nu)^{37}\text{Cl}$) and that the efficiency of these processes scales inversely with the mass. Table 7 shows the integrated flux of the main weak processes during the central O burning for two selected masses, namely the 15 and 25 M_\odot . In Table 7, the electron fraction Y_e refers to the end of oxygen burning.

EDITOR: PLACE TABLE 7 HERE.

Once oxygen is exhausted at the center, the burning moves outward and a first (main) O convective shell develops (in all the models), at a mass location corresponding roughly to the previous maximum extension of the O convective core (see Figure 8). The time duration and maximum extension reached by this first convective episode is reported in Table 2 for the four masses. Once this first O convective shell vanishes, a second one forms at a mass coordinate more internal than the previous one; the reason has already been discussed in detail in Paper I (see section 3.5 and Figure 13 of Paper I) for the 25 M_\odot and holds also for the 13 , 15 and 20 M_\odot . The last O convective shell forms almost simultaneously to the first silicon convective shell, the only exception being the 13 M_\odot model. The duration of this last oxygen convective episode is rather short, i.e. of the order of 10^{-4} yr (see Table 2) but it is rather important since it extends up to almost the base of the C burning shell, with the consequence that the Ne shell is pushed outward and squeezed towards the C one. The final location both in mass and radius of the oxygen burning shell is reported in Table 2.

3.7. Si burning

Silicon burning takes place when the central temperature reaches about $2.3 \cdot 10^9$ K. The time elapsed since the central oxygen exhaustion ranges between 160 days for the $13 M_{\odot}$ and 11 days for the $25 M_{\odot}$. The degree of neutronization at the beginning of the Si burning (see Table 3) scales inversely with the initial mass of the stars (because both the density and the evolutionary timescales scale inversely with the masses) and constitutes an important "boundary condition" since the Si burning is largely affected by such an initial neutronization (it controls at a large extent the nuclear species which will be favored in the further evolutionary phases).

Quite in general, the central Si burning phase may be divided in two phases: the first one in which Si burns radiatively and a second one in which it occurs in a convective environment.

In the $13 M_{\odot}$ case the first "radiative" phase is characterized by the total destruction of ^{28}Si and by a build up of ^{30}Si up to a maximum mass fraction of more than 0.8. At this point a convective core appears and the abundance of ^{28}Si increases again as a consequence of the advancing of the convective core in a region in which ^{28}Si is abundant (it is still the one left by the O convective core). However the ^{28}Si abundance never exceeds the ^{30}Si one, which remains the most abundant silicon isotope up to the end of this burning phase, because of the high degree of neutronization existing within the convective core. The maximum mass size of the convective core is $\simeq 1 M_{\odot}$ and the matter emerging from this burning is formed by more than 70% (by mass) of ^{52}Cr and ^{56}Fe , the first one being largely the most abundant of the two. For sake of completeness we report in Table 3 the abundances of the most abundant nuclear species during the central Si burning at three selected points: the end of the radiative phase, the moment at which ^{28}Si reaches its maximum abundance during the convective phase and the end of the central Si burning phase. The electron fraction is also reported.

As we move upward in mass, i.e. to the $15 M_{\odot}$, the development of the Si burning changes as a consequence of the reduction in the average neutronization. During the first radiative burning, ^{28}Si is largely destroyed (but no more completely) and ^{30}Si is builded up to a maximum mass fraction of $\simeq 0.675$. Once the convective core forms and begins to advance in mass, it enters a region in which the ^{28}Si is abundant and the neutron excess is low: the result is now that the ^{28}Si grows up to a value of $\simeq 0.347$, becoming the most abundant Si isotope. During all the convective phase ^{30}Si remains largely underabundant with respect to ^{28}Si . Once again at the end of central Si burning, most of the matter ($\simeq 83\%$ by mass) is concentrated in ^{52}Cr and ^{56}Fe but this time the two nuclear species have more or less the same abundance by mass. The detailed (main) abundances at selected points along the Si burning are shown in Table 3. The maximum size reached by the convective core is, also in this case, $\simeq 1 M_{\odot}$.

The trend which comes out by a comparison between the evolution of the $13 M_{\odot}$ and the $15 M_{\odot}$ is confirmed and reinforced by an analysis of the Si burning in the two more massive stellar models, i.e. the $20 M_{\odot}$ and the $25 M_{\odot}$. In fact, as the stellar mass increases, the amount of ^{28}Si burned during the first radiative phase reduces progressively so as the maximum abundance reached by the ^{30}Si . In particular ^{30}Si grows up to 0.25 in the $20 M_{\odot}$ and only up to 0.2 in the $25 M_{\odot}$, while ^{28}Si is only mildly depleted in this phase. As soon as the convective core forms, ^{30}Si almost disappears as a consequence of the low degree of neutronization existing within the whole core of both the masses. The final composition is dominated once again (more than $\simeq 85\%$ by mass) by ^{52}Cr and ^{56}Fe , the iron isotope being now the most abundant of the two (see Table 3). Note that also these two stellar models form a convective core of the order of $\simeq 1 M_{\odot}$.

The main weak interactions which drive the progressive neutronization of the matter from the central Si ignition onward are reported in Table 8 for two representative cases, i.e.

the 15 and the 25 M_{\odot} models. In particular we report in the table, for each process, the integrated effective flux and the φ parameter. The integrated effective flux is defined as:

$$\int |r_{ik} - r_{jl}| dt \quad (1)$$

where r_{ik} and r_{jl} are the forward and reverse rate of the process $i(k, j)l$; such a quantity is an estimate of the global efficiency of a certain process over a given time interval. The φ parameter is defined (see also Paper I) as:

$$\varphi(ij) = \frac{|r_{ik} - r_{jl}|}{\max(r_{ik}, r_{jl})} \quad (2)$$

and gives an estimate of the balance between the forward and reverse rate of the process $i(k, j)l$.

EDITOR: PLACE TABLE 8 HERE.

For sake of clearness Table 8 is divided into three panels: the first one refers to the central convective Si burning, the second one concerns the phase extending from the central Si exhaustion up to the onset of the Nuclear Statistical Equilibrium (NSE) and the last one refers to the final phase up to the last computed model. The last row at the end of each panel shows the process having the maximum integrated effective flux. Let us note that the most efficient weak processes during these phases are always electron captures on heavy nuclei and that these processes are far away from the equilibrium before the NSE is reached. Only during the last evolutionary stages some of these weak reactions begin to be counterbalanced by their reverse process like, e.g., the $^{52}\text{Cr}(e^-, \nu)^{52}\text{V}$ in the $15 M_{\odot}$ or the $^{59}\text{Co}(e^-, \nu)^{59}\text{Fe}$ in the $25 M_{\odot}$.

Once Si is exhausted in the center the burning shifts in a shell. In spite of the very short time available for these models before the beginning of the final collapse (and, possibly, a

successful explosion), almost 6 hours for the $13 M_{\odot}$ and only 0.5 hours for the $25 M_{\odot}$, the Si burning shell has time to move significantly outward in mass and even to produce (in all the four masses) a series of subsequent convective episodes. The first one (or two, depending on the initial mass) occurs always within the maximum extension previously reached by the convective core and is due to the presence of the small amount of Si left by the receding convective core. The following one(s) extends, on the contrary, well outside of the border of the convective core. The maximum extension in mass reached by the outer border of this convective Si shell is a very crucial quantity since it marks the discontinuity which divides the highly neutronized matter (the internal one) from the almost untouched one (the external one). This discontinuity, usually referred to as the "Fe" core mass, plays a pivotal role in the following evolution of the star, i.e. during the explosive phase. In fact it marks the limiting mass within which the shock wave loses a great deal of its energy ($\sim 10^{51}$ erg/0.1 $M_{\odot, \text{Fe}}$, see (Hillebrandt and Müller) 1981 and references therein for a more detailed discussion) through the photodisintegration of heavy nuclei. This means that the smaller is the "Fe" core mass the largest is the probability of obtaining a successful explosion. Secondly, since even a mild neutronization ($Y_e \simeq 0.49$) leads always to an NSE distribution which has a negligible abundance of ^{56}Ni , the region outside the "Fe" core is the only one in which a large amount of ^{56}Ni may be produced during the explosion. We find that in all the three more massive models the maximum extension in mass of the convective shell is rather similar (it varies between $1.43 M_{\odot}$ and $1.55 M_{\odot}$) while in the $13 M_{\odot}$ model the convective shell only marginally extends above the previous convective core, so that the final "Fe" core mass is $1.29 M_{\odot}$.

The nucleosynthesis occurring in the shell Si burning phase is basically the same already discussed in Paper I for the $25 M_{\odot}$, i.e., the Si burning shell leaves a chemical composition mainly enriched in ^{54}Fe and ^{56}Fe in proportions which differ from one model to the other; the difference between the central and the shell Si burning is mainly due to a difference in both the entropy and the neutron excess at which the nuclear burning occurs (see Paper I

for more details).

The final location in mass and radius of the silicon burning shell is reported in Table 2.

4. Discussion

The interplay between the various central and shell nuclear burnings and the temporal behavior of all the convective zones leads to final presupernova structures whose main properties are shown in Figures 11, 12, 13, 14, 15 and 16 and in the last section of Table 2.

EDITOR: PLACE FIGURE 11 HERE.

EDITOR: PLACE FIGURE 12 HERE.

EDITOR: PLACE FIGURE 13 HERE.

EDITOR: PLACE FIGURE 14 HERE.

EDITOR: PLACE FIGURE 15 HERE.

EDITOR: PLACE FIGURE 16 HERE.

Figures 11 and 12 show, respectively, the final radius-mass and density-mass relations obtained for the four stellar models; how it has been already shown by (Arnett) (1996), these

relations tend to progressively approach each other as one moves towards the center. This simply means that the more advanced the evolutionary phase the lesser is the influence of the initial mass. This occurrence is evident also in Figure 16 where the various final core masses (or, equivalently, the final location of the various burning fronts) are plotted as a function of the initial mass: the more internal core masses show clearly a shallower dependence on the initial mass than the more external ones. For example, while the final location of the H shell (i.e. the He core mass) in the $25 M_{\odot}$ is about 2.4 times larger than in the $13 M_{\odot}$, the mass location of the Si shell (i.e. the most internal one) in the $25 M_{\odot}$ is only 1.4 times larger than that of the $13 M_{\odot}$.

Figure 13 shows the final electron fraction (Y_e) profile within the inner $2 M_{\odot}$ for all the computed models. A main jump in Y_e is present between 1.3 and $1.55 M_{\odot}$ depending on the initial mass of the star; it is determined by the outer border of the convective Si burning shell since the region affected, even partially, by the Si burning experiences a rather strong neutronization. The mass within this main jump in Y_e , i.e. the iron core, is presumed to remain locked within the remnant on the basis of nucleosynthetic restrictions (see (Weaver and Woosley) 1978 and (Woosley and Weaver) 1995 for more details). The region outside the iron core mass, on the contrary, will be in large part ejected in the interstellar medium by the explosion. Actually the exact location marking the region which will be successfully ejected is at present largely unknown and constitutes one of the main uncertainties in the computation of the final explosive yields (see, e.g., (14) 1996). The Y_e profile which is present outside the iron core mass is due to the superposition of two successive episodes of neutronization. The first one occurs during the He burning and is due to the transformation of ^{14}N , left by the H burning, into ^{22}Ne : this first episode leaves a Y_e profile almost flat within all the region involved by the He burning and it is independent on the initial mass of the star (in fact the amount of ^{22}Ne produced is always equal to the total amount of ^{14}N available which, in turn, equates the initial global abundance of the isotopes involved in the CNO

cycle which obviously depends only on the initial metallicity). The second episode occurs during the convective O burning shell since both the C and Ne burnings do not produce any appreciable amount of neutronized matter. At variance with the first episode this time the degree of neutronization is a strong function of the initial mass and largely decreases as the initial mass increases. In both our two more massive stars the O shell burning does not produce an appreciable further neutronization and hence the Y_e profile remains practically flat outside the iron core mass. In the two less massive stars, on the contrary, the convective O burning shell induces an appreciable amount of neutronization; hence the final Y_e profile outside the iron core will depend on the mass extension of both the O and the Si convective shells. In particular in the $13 M_\odot$ case we find that the last Si convective episode is not able to extend up to the outer border of the previously existing O convective shell and hence part of the partially neutronized matter produced by the O shell remains outside the iron core. In the $15 M_\odot$ case the last Si convective shell extends above the previous O convective shell and hence in this case the partially neutronized matter produced by the O shell is fully engulfed by the advancing Si shell. As a consequence, in this case, the Y_e profile outside the iron core is almost flat.

For sake of completeness Figures 14 and 15 show, respectively, the specific entropy per baryon ($S/N_A k$) and the various contributions to the total pressure (i.e. radiation, ions, electrons and Coulomb interactions) for the four presupernova models. Note that the specific entropy is computed only for $T > 10^6$ K where the matter is assumed to be completely ionized. Figure 15 clearly shows that within the iron core the star is supported mainly by the degenerate electrons while outside the iron core the radiation contributes, or even dominates, in sustaining the stellar model: the contribution of the Coulomb interactions to the total pressure is in all four cases largely negligible.

Turning now to the chemical structure of the four presupernova models, Figure 17 shows the profiles of the main isotopes as a function of the internal mass;

EDITOR: PLACE FIGURE 17 HERE.

it can be easily recognized the onion structure left by the various burnings and it is also possible to determine the mass layers, summarized in Table 9, which experienced the nuclear burnings up to a given one.

EDITOR: PLACE TABLE 9 HERE.

To be more specific, the label to the left of Table 9 reports up to which burning (included) the matter between the two bracketing masses on the right has been exposed. For example the mass between $1.754 M_{\odot}$ and $1.643 M_{\odot}$ in the $15 M_{\odot}$ has been processed up to the Ne burning included. Note that the zone affected by the central H burning extends up to the surface because of the effect of the dredge up. Tables 10-13 schematically show the percentage of the abundance of each isotope present within each of the mass zones reported in Table 9. Note that the sum of the percentages does not always equal 100 because the decimal part of each fraction has been rounded off in the printout format. The last column in each of these four tables shows the final preexplosive yield of each isotope computed up to the border of the iron core.

EDITOR: PLACE TABLE 10 HERE.

EDITOR: PLACE TABLE 11 HERE.

EDITOR: PLACE TABLE 12 HERE.

EDITOR: PLACE TABLE 13 HERE.

A comparison between the present evolutions and similar computations available in literature is a very difficult task since most of the work devoted to the evolution of massive stars contains very few details on the presupernova models. The comparison between the results obtained by different authors is almost always limited to the final, explosive, yields. However, by looking in the literature of the last decade we were able to collect some data on the presupernova models of massive stars; they refer, essentially, to: (Nomoto and Hashimoto) (1988) (hereinafter NH88), (Woosley and Weaver) (1995) (hereinafter WW95), and (1) (1996) (hereinafter APB96).

Figure 18 shows the comparison of the final location in mass of the various nuclear burning shells for the 13, 15, 20 and 25 M_{\odot} , with WW95 (filled triangles), NH88 (filled squares) and APB96 (asterisk). In the following we will simply underline the similarities and the differences among the different sets of models. A real explanation of the causes of the differences existing among the various sets of models would be a too tough job either because of the lack of published data and because of the intrinsic difficulty in performing such an analysis.

EDITOR: PLACE FIGURE 18 HERE.

The upper left panel in this figure collects the final He core masses obtained by the quoted papers. This quantity is of paramount importance since, once the H is exhausted in the center, the evolution of a stellar model depends essentially on the mass size of the He core

and not any more on the total mass of the star. The comparison between our results and the NH88 ones is not meaningful because they start their computations from pure He cores; however, the fact that both of us have similar He cores will allow a meaningful comparison of the more advanced evolutionary phases. The $20 M_{\odot}$ stellar model computed by APB96 closely matches our corresponding He core mass, and this agrees with the fact that both of us adopt the Schwarzschild criterion to define the border of the convective zones. The comparison with WW95 is somewhat controversial in the sense that their $15 M_{\odot}$ is in close agreement with the present one while their $25 M_{\odot}$ forms a significantly larger core (by $\simeq 1 M_{\odot}$) respect to our. Since WW95 adopt a mild amount of overshooting ($\simeq 0.25 H_P$) we would expect their final He core masses to be systematically larger than ours. Though one could imagine the overshooting to be more effective in the $25 M_{\odot}$ rather than in the $15 M_{\odot}$, some test computations we have performed seem to exclude such a possibility.

The upper right panel in figure 18 shows the comparison among the final CO core masses. The NH88 CO core masses for the 13 , 15 and $20 M_{\odot}$ models closely match our findings while they obtain a significantly larger CO core for the $25 M_{\odot}$ star in spite of the fact that both have a similar He core and none of us includes the mechanical overshooting. APB96 obtain a significantly larger CO core (for their $20 M_{\odot}$); this occurrence can be easily explained since they clearly state that they find, and do not dump, some breathing pulses ((Castellani et al.) 1985 and (Caputo et al.) 1989) whose main effect, as it is well known, is to increase both the mass of the CO core and the He burning lifetime. WW95 obtain larger CO cores as a result of the larger He core masses and of the larger He convective cores due to the mechanical overshooting adopted during the central He burning.

The final mass location of the C burning shell coincides with the base of the last carbon convective shell where the nuclear energy production due to carbon burning reaches its

maximum. It is worth noting, however, that the main changing from a C rich layer (i.e. the CO core) to a Ne rich one (i.e. the ONe core) occurs at the outer border of the last C convective shell (see Figure 17). By the way let us note that, in general, while the final structure of the star depends on the location in mass of the active burning shells (as discussed above), the final stellar yields are sensitive to the size of the various core masses (see below). From the middle left panel of Figure 18, in which the final location of the ONe core (rather than the location of the C burning shell) is plotted, it is clear that WW95, NH88 and APB96 are in a rather good agreement among them. Our lower mass models (namely the 13 and the $15 M_{\odot}$) are in agreement with both WW95 and NH88, while our higher masses show a significantly smaller ONe cores. This is due to the fact that the our two more massive stellar models form systematically a smaller C convective shell (Table 14).

EDITOR: PLACE TABLE 14 HERE.

The behavior of the carbon convective shell directly influences the temporal evolution of the Ne burning shell since it acts as a barrier for the advancing Ne shell itself. The large difference between the $25 M_{\odot}$ star by WW95 and our corresponding model seems to indicate that in the WW95 model the carbon convective shell vanishes at a certain point of the evolution and allows the neon burning shell to advance in mass. On the contrary in our $25 M_{\odot}$ the carbon convective shell is active up to the end of the evolution keeping the Ne shell more internal. NH88 give no data on the location in mass of the Ne shell, however by comparing the final location of the O burning shell it is possible to guess that NH88 obtain a temporal evolution of the carbon convective shell similar to the one we found. APB96 stop the evolution of their $20 M_{\odot}$ to the end of central Ne burning and hence do not have data for the final location of both the Ne and O burning shells. The comparison among the various final mass locations of the O shell shows that while the NH88 models fairly agrees with the

present ones, the WW95 models end up with an O shell systematically more external than in our models.

A last important quantity we can compare is the final size of the iron core, which is directly connected to the extension in mass of the last silicon convective shell (see Paper I for more details). A comparison with NH88 shows that we obtain iron cores for the 13, 15 and $20 M_{\odot}$, systematically more massive and that this trend changes for the $25 M_{\odot}$ since NH88 find a silicon convective shell ($1.61 M_{\odot}$) more external than in our case ($1.54 M_{\odot}$) in spite of a smaller oxygen exhausted core. WW95 obtain iron core masses systematically larger than the ones we find (but in the $15 M_{\odot}$), occurrence which is consistent with the fact that they obtain in general core masses larger than ours.

A comparison between Figure 13 and Figures 2a, 2b, 2c and 2d in (14) (1996) allow also the checking of the Y_e profile just outside the edge of the iron core: also in this case significant differences are present. In particular: 1) the outer edge of the partially neutronized region in the $13 M_{\odot}$ model computed by NH88 is more external in mass ($\simeq 1.5 M_{\odot}$) and Y_e is lower ($Y_e \simeq 0.491$) than in our corresponding model, probably because of a more extended O convective shell; 2) a partially neutronized region is preserved between 1.31 and $\simeq 1.38 M_{\odot}$ in the $15 M_{\odot}$ by NH88, at variance with our corresponding model in which, as discussed above, Y_e jumps from 0.486 , within the iron core, to 0.498 outside; this occurrence should be the consequence of a less extended Si convective which is not able, as in our model, to ingest all the O convective shell; 3) in the $20 M_{\odot}$ by NH88 the outer edge of the partially neutronized region is more internal ($\simeq 1.64 M_{\odot}$) and Y_e is lower ($Y_e \simeq 0.494$) than in our corresponding model; in this case, at variance with the $13 M_{\odot}$, this should be the consequence of a less extended O convective shell; 4) the $25 M_{\odot}$ by NH88 does not show any partially neutronized region, at variance with our corresponding model; this occurrence happens probably because of an extended Si convective shell which is able to ingest all the O convective shell, similarly

to what happens in our $15 M_{\odot}$ model. The impact of these differences on the final explosive nucleosynthesis will be addressed in a forthcoming paper.

A comparison of the presupernova nucleosynthesis with similar data available in literature is a difficult task because neither NH88 nor WW95 present the preexplosive yields of their models (indeed WW95 give the preexplosive yields only in one case, i.e., the $25 M_{\odot}$ of solar chemical composition). A comparison with ABP96 is not meaningful because they stop their computation at the central Ne exhaustion. Note that they claim that above $1.9 M_{\odot}$, in the $20 M_{\odot}$ model, the chemical composition does not change significantly because of the very short evolutionary timescales of the more advanced phases, and hence they compare the abundances of isotopes up to ^{27}Al with WW95 and NH88; actually we find that isotopes heavier than ^{17}O suffer substantial modifications even after central Ne exhaustion. Table 15 shows a comparison of the presupernova yields (in M_{\odot}) of the isotopes lighter than $A=27$ to the ones computed at the central Ne exhaustion. In the last column of Table 15 we report the site in which the various isotopes are modified after the central Ne exhaustion; the labels "p" and "d" indicating respectively whether each isotope is produced or destroyed.

EDITOR: PLACE TABLE 15 HERE.

5. Summary and Conclusions

In this paper, which is the second of the series, we have presented and discussed in some detail the presupernova evolution of four stellar masses having solar chemical composition. All the various burning phases have been studied by adopting a very extended network fully embedded into the stellar evolutionary code (FRANEC). A comparison of our results with similar ones available in the literature shows that, in spite of an overall similarity, the existing

differences are significant and at present not completely understood.

One of us (A.C.) thanks the Astronomical Observatory of Rome and its Director, Prof. Roberto Buonanno, for the generous hospitality at Monteporzio Catone. This paper has been partially supported by the MURST (COFIN98).

A. Explosive nucleosynthetic yields

In this appendix we anticipate the elemental explosive nucleosynthetic yields coming from a set of models including the present ones and those of lower metallicity, i.e., $Z = 0$ ($Y = 0.23$) and $Z = 10^{-3}$ ($Y = 0.23$). The explosion has been obtained by depositing at the border of the iron core an amount of energy equal to $1.2 \cdot 10^{51}$ erg plus the binding energy. Each table refers to a single mass and each column refers to a different choice of the mass cut (i.e., for a different choice of the ejected ^{56}Ni). The last column refers to a mass cut equal to the iron core mass (which also corresponds to the maximum amount of ^{56}Ni available). All the unstable isotopes have been decayed into their parent stable nuclei. These results will be discussed in detail in a forthcoming paper.

EDITOR: PLACE TABLE 16 HERE.

EDITOR: PLACE TABLE 17 HERE.

EDITOR: PLACE TABLE 18 HERE.

EDITOR: PLACE TABLE 19 HERE.

EDITOR: PLACE TABLE 20 HERE.

EDITOR: PLACE TABLE 21 HERE.

EDITOR: PLACE TABLE 22 HERE.

EDITOR: PLACE TABLE 23 HERE.

EDITOR: PLACE TABLE 24 HERE.

EDITOR: PLACE TABLE 25 HERE.

EDITOR: PLACE TABLE 26 HERE.

REFERENCES

Arnett, W.A. 1972, *ApJ*, 176, 681

Arnett, W.A. 1996, in *Supernovae and Nucleosynthesis*, ed. J.P. Ostriker (Princeton: Princeton Univ. Press)

Aubert, O., Prantzos, N., and Baraffe, I. 1996, *A&A*, 312, 845

Beaudet, G., Petrosian, V., and Salpeter, E.E. 1967, *ApJ*, 150, 979

Caputo, F., Chieffi, A., Tornambè, A., Castellani, V., and Pulone, L. 1989, *ApJ*, 340, 241

Castellani, V., Chieffi, A., Pulone, L., and Tornambè, A. 1985, *ApJ*, 296, 204

Caughlan, G.R., Fowler, W.A., Harris, M., and Zimmerman, B. 1985, *At. Data Nucl. Data Tables*, 32, 197

Chieffi, A., and Straniero, O. 1989, *ApJS*, 71, 48

Chieffi, A., Limongi, M., and Straniero, O. 1998, *ApJ*, 502, 737 (Paper I)

Cox, J.P., and Giuli, R.T. 1968, in *Principles of Stellar Evolution*, Vol. 1, (New York:Gordon and Breach), 281

De Witt, H., Graboske, H., and Cooper, M. 1973, *ApJ*, 181, 439

Dicus, D.A., Kolb, E.D., Schramm, D.N., and Tubbs, D.L. 1976, *ApJ*, 210, 481

Festa, G.G., and Rudermann, M.A. 1969, *Phys. Rev. A*, 180, 1227

Fuller, G.M., Fowler, W.A., and Newman, M. 1980, *ApJS*, 42, 447

Fuller, G.M., Fowler, W.A., and Newman, M. 1982, *ApJS*, 48, 279

Fuller, G.M., Fowler, W.A., and Newman, M. 1985, *ApJ*, 293, 1

Graboske, H., De Witt, H., Grossman, A., and Cooper, M. 1973, *ApJ*, 181, 457

Grevesse, N. in *Evolution of Stars: The Photospheric Abundance Connection*, ed. G. Michaud and A. Tutukov, (Dordrecht:Kluwer), 63, 1991

Hillebrandt, W. and Müller, E. 1981, *A&A*, 103, 147

Huebner, W.F., Merts, A.L., Magee, N.H., and Argo, M.F. 1977, Los Alamos Sci. Lab. Rept. (LA-6760-M) (LAOL)

Kurucz, R.L. 1991, in *Stellar Atmospheres: Beyond Classical Model*, ed. L. Crivellari, I. Hubeny, and D.G. Hummer (Dordrecht:Kluwer), 441

Iglesias, C.A., Rogers, F.J., and Wilson, B.G. 1992, *ApJ*, 397, 717 (OPAL)

Itoh, N., Totsuji, H., and Ichimaru, S. 1977, *ApJ*, 218, 477

Itoh, N., Totsuji, H., Ichimaru, S., and De Witt, H. 1979, *ApJ*, 234, 1079

Itoh, N., Mitake, S., Iyetomi, H., and Ichimaru, S. 1983, *ApJ*, 273, 774

Langer, N., El Eid, M., and Baraffe, I. 1989, *A&A*, 224, L17

Munakata, H., Kohyama, Y., and Itoh, N. 1985, *ApJ*, 296, 197

Munakata, H., Kohyama, Y., and Itoh, N. 1986, *ApJ*, 304, 580

Nomoto, K., and Hashimoto, M. 1988, *Phys. Rep.*, 163, 13

Richardson, M.B., Van Horne, H.M., Ratcliff, K.F., and Malone, R.C. 1982, *ApJ*, 255, 624

Straniero, O. 1988, *A&AS*, 76, 157

Straniero, O., Chieffi, A., and Limongi, M. 1997, *ApJ*, 490, 425

Thielemann, F.K., and Arnett, W.D. 1985, *ApJ*, 295, 604

Thielemann, F.K., Nomoto, K., and Hashimoto, M. 1996, ApJ, 460, 408

Weaver, T.A., and Woosley, S.E. 1978, ApJ, 225, 1021

Weaver, T.A., and Woosley, S.E. 1993, Phys. Rep., 227, 65

Woosley, S.E., Arnett, W.A., and Clayton, D.D. 1972, ApJ, 175, 731

Woosley, S.E., and Weaver, T.A. 1986, ARA&A, 24, 205

Woosley, S.E., and Weaver, T.A. 1995, ApJS, 101, 181

FIGURE CAPTIONS

Fig. 1.— Path followed by the computed models in the HR diagram.

Fig. 2.— Path followed by the computed models in the $\log T_c - \log \rho_c$ diagram; the various nuclear burning ignitions are shown in the figure.

Fig. 3.— Temporal behaviour of the convective zones for the computed models from the MS phase up to the central carbon ignition.

Fig. 4.— Temporal evolution of the radius of the internal mass layers in steps of $1 M_\odot$ from the H exhaustion to the presupernova stage for the four computed models. The dashed lines refer to the mass location of the H (the more external one) and of the He (the more internal one) burning shells.

Fig. 5.— Temporal evolution of the surface effective temperature as a function of the central He mass fraction.

Fig. 6.— Evolution of both the radius (*upper panel*) and the mass (*lower panel*) of the H burning shell (defined as the mass corresponding to the maximum energy generation rate provided by the H burning reactions) as a function of the central temperature up to the presupernova stage. The *solid lines* refer to the $13 M_\odot$ model, the *dotted lines* to the $15 M_\odot$ model, the *dashed lines* to the $20 M_\odot$ model and the *long dashed lines* to the $25 M_\odot$ model.

Fig. 7.— Temporal behaviour of the various luminosities: photons (*dashed lines*), neutrinos (*dotted lines*) and nuclear (*solid lines*). The carbon burning ignition is indicated in each panel by the big filled dot labeled as "C".

Fig. 8.— Temporal behaviour of the convective zones for all the computed models from the central He exhaustion up to the presupernova stage.

Fig. 9.— Evolution of central ^{12}C mass fraction (*panel a*), central density (*panel b*), central nuclear generation rate (*panel c*) and neutrino losses (*panel d*) as a function of the central temperature for both the 15 (*solid line*) and the 25 M_\odot (*dashed line*) during central carbon burning. The vertical *dotted line* marks the formation of the convective core in the 15 M_\odot .

Fig. 10.— Evolution of the mass location of the C burning shell superimposed to the convective zones as a function of time from central C burning to the presupernova stage.

Fig. 11.— Presupernova radial profile as a function of the interior mass for all the computed models.

Fig. 12.— Presupernova density profile as a function of the interior mass for all the computed models.

Fig. 13.— Presupernova electron fraction profile as a function of the interior mass within the inner 2 M_\odot for all the computed models.

Fig. 14.— Presupernova profile of the specific entropy per barion as a function of the interior mass. Note that the specific entropy per barion is computed only for temperatures larger than 10^6 K , where the matter is assumed to be completely ionized.

Fig. 15.— Various contributions to the total pressure within the He core of all the presupernova models: radiation (*solid lines*), ions (*dotted lines*), electrons (*dashed lines*), Coulomb corrections (*long dashed lines*).

Fig. 16.— Final location of the various core masses (or equivalently of the various nuclear burning shells) for all the computed models: H (*open stars*), He (*skeletal stars*), C (*filled triangles*), Ne (*open squares*), O (*filled squares*), Si (*filled circles*), Iron Cores (*open circles*).

Fig. 17.— Internal profiles of the most abundant nuclear species for all the presupernova models.

Fig. 18.— Comparison of the final location in mass of the various nuclear burning shells of all the presupernova models with WW95 (*filled triangles*), NH88 (*filled squares*) and APB96 (asterisk).

TABLE 1
NUCLEAR NETWORK ADOPTED IN THE CALCULATIONS

Element	A _{min}	A _{max}	Element	A _{min}	A _{max}
n	1	1	S	31	37
H	1	3	Cl	33	37
He	3	4	Ar	36	41
Li	6	7	K	37	42
Be	7	10	Ca	40	49
B	10	11	Sc	41	49
C	12	14	Ti	44	51
N	13	16	V	45	52
O	15	19	Cr	48	55
F	17	20	Mn	51	57
Ne	20	23	Fe	52	61
Na	21	24	Co	55	61
Mg	23	27	Ni	56	65
Al	25	28	Cu	57	66
Si	27	32	Zn	64	68
P	29	34			

TABLE 2
SELECTED QUANTITIES FOR $13 M_{\odot}$, $15 M_{\odot}$, $20 M_{\odot}$ AND $25 M_{\odot}$ MODELS.

	$13 M_{\odot}$	$15 M_{\odot}$	$20 M_{\odot}$	$25 M_{\odot}$
H Burning				
τ_H (yr)	1.25(7)	1.07(7)	7.48(6)	5.93(6)
M_{cc} (M_{\odot})	4.92	6.11	9.30	13.77
Δt H conv shell (yr)	6.4(4)	4.8(4)	8.9(5)	8.2(5)
ΔM H conv shell (M_{\odot})	2.50-5.60	3.32-6.33	4.71-10.69	6.74-15.95
$M_{H \text{ shell}}^{\text{final}}$ (M_{\odot})	3.42	4.20	6.00	8.10
$M_{\text{He core}}^{\text{final}}$ (M_{\odot})	3.33	4.10	5.94	8.01
$R_{H \text{ shell}}^{\text{final}}$ (R_{\odot})	2.00	1.00	6.80(-1)	6.70(-1)
$R_{\text{He core}}^{\text{final}}$ (R_{\odot})	1.42	6.70(-1)	6.00(-1)	5.66(-1)
Convective Envelope				
$M_{\text{conv. env.}}^{\text{final}}$ (M_{\odot})	3.48	4.28	6.15	8.27
$^{12}\text{C}/^{13}\text{C}$	18	93	91	90
$^{14}\text{N}/^{15}\text{N}$	1948	2132	2702	2977
$^{16}\text{O}/^{17}\text{O}$	745	881	919	1052
$^{16}\text{O}/^{18}\text{O}$	568	565	574	572
He Burning				
Δt (H exh.-He ign.)	5.47(4)	3.70(4)	1.89(4)	1.16(4)
τ_{He} (yr)	1.9(6)	1.4(6)	9.3(5)	6.8(5)
M_{cc} (M_{\odot})	1.73	2.33	3.63	5.23
$^{12}\text{C}/^{16}\text{O}$	0.257/0.717	0.195/0.777	0.171/0.800	0.179/0.790
Δt 1 He conv shell (yr)	3.0(2)	3.8(4)	2.2(3)	6.2(3)
ΔM 1 He conv shell (M_{\odot})	1.94-2.03	2.50-2.88	3.86-4.54	5.46-6.45
Δt 2 He conv shell (yr)	1.7(2)	1.9(3)	1.18(3)	2.37(3)
ΔM 2 He conv shell (M_{\odot})	1.75-3.08	2.43-3.54	3.73-5.64	5.30-7.68
$^4\text{He}_{\text{shell}}$	0.809	0.858	0.863	0.877
$^{12}\text{C}_{\text{shell}}$	8.95(-2)	8.36(-2)	8.49(-2)	8.04(-2)
$^{16}\text{O}_{\text{shell}}$	7.47(-2)	3.23(-2)	2.59(-2)	1.67(-2)
$^{18}\text{O}_{\text{shell}}$	5.23(-4)	1.92(-3)	4.86(-4)	4.81(-4)
$^{22}\text{Ne}_{\text{shell}}$	1.82(-2)	1.82(-2)	2.01(-2)	2.01(-2)
$^{25}\text{Mg}_{\text{shell}}$	9.07(-4)	9.55(-5)	1.23(-4)	9.49(-5)
$^{56}\text{Fe}_{\text{shell}}$	9.17(-4)	1.15(-3)	1.13(-3)	1.13(-3)
$M_{\text{He shell}}^{\text{final}}$ (M_{\odot})	1.75	2.43	3.73	5.31
$M_{\text{CO core}}^{\text{final}}$ (M_{\odot})	1.75	2.39	3.44	4.90
$R_{\text{He shell}}^{\text{final}}$ (R_{\odot})	2.18(-2)	4.00(-2)	4.63(-2)	7.12(-2)
$R_{\text{CO core}}^{\text{final}}$ (R_{\odot})	2.18(-2)	3.41(-2)	2.92(-2)	5.22(-2)

TABLE 2—*Continued*

	13 M _⊙	15 M _⊙	20 M _⊙	25 M _⊙
C Burning				
Δt (He exh.-C ign.)	5.94(4)	3.67(4)	2.16(4)	1.59(4)
τ_{C} (yr)	4.8(3)	2.6(3)	1.45(3)	9.7(2)
M_{cc} (M _⊙)	0.56	0.41		
Δt ₁ C conv shell (yr)	6.30(2)	2.40(2)	2.80	5.64
ΔM ₁ C conv shell (M _⊙)	0.55-1.10	0.39-0.80	1.07-1.50	1.48-2.43
Δt ₂ C conv shell (yr)	60	56	2.16	0.34
ΔM ₂ C conv shell (M _⊙)	0.92-1.42	0.80-1.20	1.46-2.64	2.28-4.61
Δt ₃ C conv shell (yr)	8.7	13	3.8(-4)	
ΔM ₃ C conv shell (M _⊙)	1.25-1.64	1.18-1.77	2.39-2.77	
Δt ₄ C conv shell (yr)	1.32(-2)	0.7		
ΔM ₄ C conv shell (M _⊙)	1.52-1.75	1.56-1.67		
Δt ₅ C conv shell (yr)		0.32		
ΔM ₅ C conv shell (M _⊙)		1.64-2.18		
$M_{\text{C shell}}^{\text{final}}$ (M _⊙)	1.56	1.80	2.41	2.39
$R_{\text{C shell}}^{\text{final}}$ (R _⊙)	7.03(-3)	9.29(-3)	1.14(-2)	1.09(-2)
Ne Burning				
Δt (C exh.-Ne ign.)	1.52(3)	5.50(2)	3.02(2)	9.20(1)
τ_{Ne} (yr)	3.00	2.00	1.46	0.77
M_{cc} (M _⊙)	0.86	0.66	0.50	0.50
Δt ₁ Ne conv shell (yr)	3.40(-2)	0.05		
ΔM ₁ Ne conv shell (M _⊙)	0.93-1.26	0.93-1.24		
Δt ₂ Ne conv shell (yr)	1.39(-2)			
ΔM ₂ Ne conv shell (M _⊙)	1.33-1.42			
Δt ₃ Ne conv shell (yr)	8.40(-3)			
ΔM ₃ Ne conv shell (M _⊙)	1.42-1.47			
$M_{\text{Ne shell}}^{\text{final}}$ (M _⊙)	1.52	1.69	2.24	2.28
$R_{\text{Ne shell}}^{\text{final}}$ (R _⊙)	5.70(-3)	7.04(-3)	9.66(-3)	9.12(-3)
O Burning				
Δt (Ne exh.-O ign.)	2.66	0.00	0.00	0.00
τ_{O} (yr)	8.07	2.47	0.72	0.33
M_{cc} (M _⊙)	0.93	0.94	1.12	1.15
Δt ₁ O conv shell (yr)	2.8(-1)	2.0(-1)	2.8(-2)	3.0(-2)
ΔM ₁ O conv shell (M _⊙)	0.92-1.33	0.92-1.44	1.11-1.77	1.14-1.86
Δt ₂ O conv shell (yr)	1.7(-2)	1.0(-2)	2.3(-3)	1.4(-3)
ΔM ₂ O conv shell (M _⊙)	0.48-0.92	0.46-0.92	0.76-1.11	0.97-1.12
Δt ₃ O conv shell (yr)	1.4(-2)	3.0(-4)	2.3(-4)	8.0(-5)
ΔM ₃ O conv shell (M _⊙)	1.05-1.39	1.43-1.65	1.64-2.22	1.83-2.09
$M_{\text{O shell}}^{\text{final}}$ (M _⊙)	1.39	1.48	1.74	1.84
$R_{\text{O shell}}^{\text{final}}$ (R _⊙)	3.74(-3)	3.80(-3)	4.42(-2)	4.75(-3)

TABLE 2—*Continued*

	13 M _⊙	15 M _⊙	20 M _⊙	25 M _⊙
Si Burning Radiative				
Δt (O exh.-Si ign.)	4.48(-1)	1.50(-2)	3.00(-2)	3.00(-2)
$\tau_{\text{Si-rad}}$ (yr)	0.58	0.29	2.80(-2)	1.94(-2)
Log T_c	9.308-9.497	9.342-9.486	9.367-9.507	9.360-9.497
Log ρ_c	7.808-8.643	7.362-8.351	7.475-8.007	7.480-7.980
Si Burning Convective				
$\tau_{\text{Si-con}}$ (yr)	0.07	0.02	3.50(-3)	3.41(-3)
M_{cc} (M _⊙)	1.13	1.14	1.11	1.12
$\Delta t_{1 \text{ Si conv shell}}$ (yr)	1.4(-4)	1.0(-5)	2.5(-5)	1.9(-5)
$\Delta M_{1 \text{ Si conv shell}}$ (M _⊙)	0.47-0.83	0.65-0.82	0.88-1.11	0.88-1.13
$\Delta t_{2 \text{ Si conv shell}}$ (yr)	5.6(-4)	3.0(-5)	8.1(-5)	4.3(-5)
$\Delta M_{2 \text{ Si conv shell}}$ (M _⊙)	0.84-1.29	0.81-1.02	1.11-1.57	1.09-1.54
$\Delta t_{3 \text{ Si conv shell}}$ (yr)	1.3(-5)	2.3(-6)	6.9(-6)	
$\Delta M_{3 \text{ Si conv shell}}$ (M _⊙)	0.84-1.05	1.00-1.13	1.11-1.28	
$\Delta t_{4 \text{ Si conv shell}}$ (yr)		1.1(-5)		
$\Delta M_{4 \text{ Si conv shell}}$ (M _⊙)		1.02-1.43		
$M_{\text{Si shell}}^{\text{final}}$ (M _⊙)	1.09	1.29	1.43	1.54
$R_{\text{Si shell}}^{\text{final}}$ (R _⊙)	2.40(-3)	2.24(-3)	2.79(-3)	3.11(-3)
Last Model				
Log T_c	9.60	9.72	9.72	9.74
Log ρ_c	9.00	9.53	9.26	9.20
ψ_c^{a}	10.10	12.03	9.35	8.57
η_c^{b}	0.124	0.136	0.130	0.128
$Y_{\text{e},c}$	0.438	0.432	0.435	0.436
$S_c/(N_A k)$	0.438	0.432	0.435	0.436
M_{Fe} (M _⊙)	1.292	1.429	1.552	1.527
R_{Fe} (R _⊙)	2.95(-3)	3.07(-3)	3.30(-3)	3.09(-3)

^aCentral value of the degeneracy parameter^bCentral value of the neutron excess

TABLE 3

MOST ABUNDANT NUCLEAR SPECIES AT THE CENTER LEFT BY THE VARIOUS NUCLEAR BURNINGS FOR $13 M_{\odot}$, $15 M_{\odot}$, $20 M_{\odot}$ AND $25 M_{\odot}$ MODELS.

Isotope	$13 M_{\odot}$	$15 M_{\odot}$	$20 M_{\odot}$	$25 M_{\odot}$
H Burning				
^4He	0.981	0.980	0.980	0.980
^{14}N	1.32(-2)	1.33(-2)	1.33(-2)	1.33(-2)
^{20}Ne	1.67(-3)	1.66(-3)	1.66(-3)	1.66(-3)
^{21}Ne	8.40(-8)	6.98(-8)	5.35(-8)	4.58(-8)
^{22}Ne	1.01(-5)	1.21(-5)	1.77(-5)	2.32(-5)
^{23}Na	1.90(-4)	1.90(-4)	1.88(-4)	1.85(-4)
^{24}Mg	5.35(-4)	5.35(-4)	5.35(-4)	5.35(-4)
^{25}Mg	6.35(-7)	7.28(-9)	2.21(-9)	1.00(-9)
^{26}Mg	1.52(-4)	1.53(-4)	1.53(-4)	1.53(-4)
^{26}Al	1.58(-6)	1.58(-7)	2.64(-7)	4.16(-7)
^{27}Al	6.03(-5)	6.03(-5)	6.04(-5)	6.05(-5)
He Burning				
^{12}C	0.257	0.195	0.171	0.179
^{16}O	0.717	0.777	0.800	0.790
^{20}Ne	1.66(-3)	1.90(-3)	2.83(-3)	3.71(-3)
^{22}Ne	1.80(-2)	1.61(-2)	1.30(-2)	1.16(-2)
^{23}Na	2.04(-4)	2.15(-4)	2.22(-4)	2.23(-4)
^{24}Mg	4.57(-4)	4.41(-4)	4.63(-3)	4.96(-3)
^{25}Mg	1.62(-3)	2.84(-3)	4.49(-3)	5.20(-3)
^{26}Mg	1.65(-3)	2.29(-3)	4.91(-3)	5.80(-3)
^{56}Fe	6.06(-4)	3.76(-4)	2.05(-4)	1.61(-4)
^{58}Fe	3.34(-4)	4.41(-4)	4.15(-4)	3.81(-4)
η_c	1.987(-3)	1.980(-3)	1.936(-3)	1.917(-3)
Y_e	0.4990	0.4990	0.4990	0.4990
C Burning				
^{16}O	0.614	0.700	0.730	0.710
^{20}Ne	0.294	0.230	0.200	0.220
^{23}Na	2.34(-2)	1.82(-2)	1.72(-2)	1.72(-2)
^{24}Mg	2.61(-2)	1.70(-2)	1.27(-2)	1.42(-2)
η_c	2.839(-3)	2.490(-3)	2.215(-3)	2.168(-3)
Y_e	0.4986	0.4987	0.4989	0.4989

TABLE 3—*Continued*

Isotope	13 M _⊙	15 M _⊙	20 M _⊙	25 M _⊙
Ne Burning				
¹⁶ O	0.768	0.811	0.830	0.826
²⁴ Mg	8.16(-2)	4.90(-2)	4.37(-2)	4.71(-2)
²⁸ Si	8.22(-2)	7.03(-2)	6.35(-2)	6.35(-2)
²⁹ Si	2.07(-2)	1.74(-2)	1.54(-2)	1.51(-2)
³⁰ Si	9.24(-3)	1.09(-2)	1.07(-2)	1.14(-2)
³¹ P	6.17(-3)	1.24(-2)	1.02(-2)	7.77(-3)
³² S	9.48(-2)	1.33(-2)	1.34(-2)	1.52(-2)
η_c	2.685(-3)	2.543(-3)	2.272(-3)	2.156(-3)
Y_e	0.4987	0.4987	0.4989	0.4989
O Burning				
²⁸ Si	0.300	0.343	0.401	0.428
³⁰ Si	0.268	5.90(-3)	1.30(-3)	8.70(-4)
³² S	2.45(-2)	0.115	0.253	0.288
³⁴ S	0.356	0.217	7.43(-2)	5.32(-2)
³⁶ Ar	1.48(-4)	6.22(-3)	3.76(-2)	4.53(-2)
³⁸ Ar	3.77(-2)	0.210	0.151	0.115
⁴⁰ Ca	9.57(-7)	2.62(-3)	3.56(-2)	4.54(-2)
η_c	4.116(-2)	2.447(-2)	1.419(-2)	9.983(-3)
Y_e	0.4794	0.4878	0.4929	0.4950
Si Burning Radiative				
²⁸ Si	4.46(-3)	4.73(-2)	0.364	0.430
³⁰ Si	0.818	0.675	0.249	0.197
³² S	1.24(-5)	3.00(-4)	6.92(-3)	9.93(-3)
³⁴ S	7.98(-2)	0.166	0.189	0.165
³⁸ Ar	5.98(-4)	2.74(-3)	9.60(-3)	9.92(-3)
⁵⁰ Ti	6.17(-2)	1.21(-2)	3.99(-4)	2.79(-4)
⁵² Cr	8.43(-3)	7.01(-2)	0.121	0.120
η_c	6.994(-2)	6.423(-2)	4.100(-2)	3.653(-2)
Y_e	0.4650	0.4679	0.4795	0.4817
Si Burning Convective (first phase)				
²⁸ Si	0.160	0.347	0.442	0.461
³⁰ Si	0.196	0.146	4.31(-3)	2.25(-3)
³² S	3.63(-3)	1.14(-2)	6.09(-2)	7.41(-2)
³⁴ S	0.145	0.151	1.42(-2)	8.83(-3)
³⁸ Ar	8.23(-3)	1.23(-2)	4.50(-3)	3.27(-3)
⁵² Cr	0.338	0.206	9.72(-2)	6.02(-2)
⁵⁴ Fe	5.00(-4)	2.61(-3)	0.132	3.42(-2)
⁵⁶ Fe	1.09(-1)	9.29(-2)	0.154	0.112

TABLE 3—*Continued*

Isotope	13 M _⊙	15 M _⊙	20 M _⊙	25 M _⊙
Si Burning (final abundances)				
⁵⁰ Ti	4.21(-2)	1.03(-2)	1.21(-4)	1.10(-4)
⁵¹ V	2.47(-2)	1.24(-2)	1.25(-3)	1.19(-3)
⁵² Cr	0.431	0.437	0.258	0.246
⁵³ Cr	3.87(-2)	2.35(-2)	3.51(-3)	3.41(-3)
⁵⁴ Cr	7.40(-2)	2.66(-2)	7.75(-4)	7.42(-4)
⁵⁵ Mn	3.98(-2)	2.93(-2)	7.06(-3)	7.06(-3)
⁵⁴ Fe	1.53(-4)	6.56(-4)	3.05(-2)	3.24(-2)
⁵⁵ Fe	1.24(-3)	3.15(-3)	3.04(-2)	3.20(-2)
⁵⁶ Fe	0.268	0.398	0.600	0.605
⁵⁷ Fe	1.88(-2)	1.68(-2)	6.57(-3)	6.76(-3)
⁵⁸ Fe	4.16(-2)	2.20(-2)	1.59(-3)	1.60(-3)
η_c	8.283(-2)	7.731(-2)	7.100(-2)	7.053(-2)
Y_e	0.4586	0.4613	0.4645	0.4647

TABLE 4
 FINAL SURFACE ABUNDANCES FOR $13 M_{\odot}$, $15 M_{\odot}$, $20 M_{\odot}$ AND $25 M_{\odot}$
 MODELS.

Isotope	Solar	$13 M_{\odot}$	$15 M_{\odot}$	$20 M_{\odot}$	$25 M_{\odot}$
1H	6.95(-01)	6.49(-01)	6.38(-01)	6.09(-01)	5.93(-01)
3He	3.04(-05)	2.20(-05)	2.06(-05)	1.70(-05)	1.61(-05)
4He	2.85(-01)	3.31(-01)	3.42(-01)	3.71(-01)	3.87(-01)
^{12}C	3.46(-03)	2.20(-03)	2.19(-03)	2.02(-03)	1.97(-03)
^{13}C	4.16(-05)	1.25(-04)	2.36(-05)	2.23(-05)	2.19(-05)
^{14}N	1.02(-03)	3.54(-03)	3.88(-03)	4.81(-03)	5.21(-03)
^{15}N	4.03(-06)	1.82(-06)	1.82(-06)	1.78(-06)	1.75(-06)
^{16}O	1.00(-02)	8.72(-03)	8.48(-03)	7.64(-03)	7.26(-03)
^{17}O	4.04(-06)	1.17(-05)	9.62(-06)	8.31(-06)	6.90(-06)
^{18}O	2.25(-05)	1.54(-05)	1.50(-05)	1.33(-05)	1.27(-05)
^{19}F	4.21(-07)	3.43(-07)	3.31(-07)	2.65(-07)	2.49(-07)
^{20}Ne	1.68(-03)	1.68(-03)	1.68(-03)	1.68(-03)	1.68(-03)
^{21}Ne	4.29(-06)	4.00(-06)	3.80(-06)	2.97(-06)	2.72(-06)
^{22}Ne	1.35(-04)	1.16(-04)	1.14(-04)	1.08(-04)	1.07(-04)
^{23}Na	3.47(-05)	5.67(-05)	5.95(-05)	6.77(-05)	7.01(-05)
^{24}Mg	5.35(-04)	5.35(-04)	5.35(-04)	5.35(-04)	5.35(-04)
^{25}Mg	7.03(-05)	6.19(-05)	5.83(-05)	5.04(-05)	4.71(-05)
^{26}Mg	8.07(-05)	8.94(-05)	9.33(-05)	1.00(-04)	1.02(-04)
^{26}Al	0.00(+00)	1.20(-08)	2.27(-08)	8.19(-07)	1.42(-06)
^{27}Al	6.03(-05)	6.03(-05)	6.03(-05)	6.03(-05)	6.03(-05)

TABLE 5
SELECTED PROPERTIES OF THE C CONVECTIVE SHELLS FOR THE $15 M_{\odot}$ MODEL.

	(1)	(2)	(3)	(4)
^{12}C	0.160-3.96(-2)	0.150-3.66(-2)	0.168-2.89(-2)	5.00(-2)-4.82(-3)
^{20}Ne	3.61(-2)-0.197	4.77(-2)-0.203	3.39(-2)-0.212	0.186-0.222
^{22}Ne	1.38(-2)-7.89(-3)	1.29(-2)-6.86(-3)	1.31(-2)-5.25(-3)	6.39(-3)-1.66(-3)
^{23}Na	7.01(-3)-1.57(-2)	7.56(-3)-1.47(-2)	6.04(-3)-1.34(-2)	1.26(-2)-1.01(-2)
^{24}Mg	1.96(-3)-1.37(-2)	2.38(-3)-1.52(-2)	1.53(-3)-1.83(-2)	1.49(-2)-3.08(-2)
^{25}Mg	2.99(-3)-7.83(-3)	3.55(-3)-8.53(-3)	3.51(-3)-9.93(-3)	8.99(-3)-1.38(-2)
^{27}Al	1.58(-3)-3.98(-3)	1.89(-3)-4.08(-3)	1.56(-3)-4.33(-3)	3.90(-3)-5.76(-3)
n_{n}	2.16(8)-5.90(7)	7.51(8)-2.75(8)	9.36(9)-1.84(9)	2.00(12)-5.70(11)
T	7.8(8)-8.8(8)	8.9(8)-9.5(8)	9.8(8)-1.1(9)	1.2(9)-1.3(9)
ρ	3.11(5)-3.36(5)	2.50(5)-2.90(5)	2.04(5)-2.25(5)	2.28(5)-2.28(5)
$^{22}\text{Ne}(\alpha, \text{n})^{25}\text{Mg}$	1.6(19)	1.6(20)	2.6(15)	8.2(17)
$^{20}\text{Ne}(\text{n}, \gamma)^{21}\text{Ne}$	8.1(18)	1.3(20)	2.4(15)	9.1(17)
$^{25}\text{Mg}(\text{n}, \gamma)^{26}\text{Mg}$	2.3(18)	2.2(19)	4.1(14)	2.3(17)
$^{23}\text{Na}(\text{n}, \gamma)^{24}\text{Na}$	2.3(18)	1.6(19)	2.5(14)	6.8(16)
$^{21}\text{Ne}(\alpha, \text{n})^{24}\text{Mg}$	1.3(18)	5.2(19)	1.2(15)	8.0(17)
$^{24}\text{Mg}(\text{n}, \gamma)^{25}\text{Mg}$	1.1(18)	2.0(19)	4.2(14)	2.7(17)
$^{27}\text{Al}(\text{n}, \gamma)^{28}\text{Al}$	7.5(17)	5.9(18)	1.0(14)	4.4(16)
maximum integrated flux	4.0(20)	2.4(21)	3.2(16)	6.2(18)

TABLE 6
SELECTED PROPERTIES OF THE C CONVECTIVE SHELLS FOR
 $25 M_{\odot}$ MODEL.

	(1)	(2)
^{12}C	0.110-1.63(-2)	0.155-2.04(-2)
^{20}Ne	9.09(-2)-0.208	3.21(-2)-0.195
^{22}Ne	6.61(-3)-2.48(-3)	9.04(-3)-1.31(-3)
^{23}Na	9.64(-3)-1.17(-2)	4.94(-3)-9.26(-3)
^{24}Mg	4.53(-3)-1.99(-2)	1.46(-3)-2.26(-2)
^{25}Mg	6.72(-3)-1.03(-2)	5.85(-3)-1.14(-2)
^{27}Al	4.19(-3)-6.15(-3)	2.10(-3)-6.25(-3)
n_{n}	1.11(11)-2.76(10)	4.03(12)-1.10(12)
T	1.03(9)-1.23(9)	1.07(9)-1.39(9)
ρ	1.73(5)-1.24(5)	1.14(5)-1.66(5)
$^{22}\text{Ne}(\alpha, n)^{25}\text{Mg}$	2.1(15)	1.0(17)
$^{20}\text{Ne}(n, \gamma)^{21}\text{Ne}$	2.1(15)	9.4(16)
$^{21}\text{Ne}(\alpha, n)^{24}\text{Mg}$	1.4(15)	7.0(16)
$^{25}\text{Mg}(n, \gamma)^{26}\text{Mg}$	4.4(14)	2.7(16)
$^{24}\text{Mg}(n, \gamma)^{25}\text{Mg}$	3.6(14)	1.8(16)
$^{23}\text{Na}(n, \gamma)^{24}\text{Na}$	2.3(14)	9.5(15)
$^{27}\text{Al}(n, \gamma)^{28}\text{Al}$	1.5(14)	6.7(15)
maximum integrated flux	2.9(16)	9.4(17)

TABLE 7
 INTEGRATED FLUX OF THE OST EFFICIENT WEAK
 INTERACTIONS DURING CENTRAL O BURNING FOR $15 M_{\odot}$ AND
 $25 M_{\odot}$.

Reaction	$15 M_{\odot}$	$25 M_{\odot}$
$^{31}\text{S}(\beta^+)^{31}\text{P}$	6.7(19)	6.4(16)
$^{33}\text{S}(\text{e}^-, \nu)^{33}\text{P}$	1.2(19)	3.0(15)
$^{30}\text{P}(\text{e}^-, \nu)^{30}\text{Si}$	3.7(18)	9.8(14)
$^{37}\text{Ar}(\text{e}^-, \nu)^{37}\text{Cl}$	3.1(18)	2.8(15)
maximum integrated flux	5.4(21)	9.9(19)
Y_{e}	0.488	0.495

TABLE 8
MOST EFFICIENT WEAK INTERACTIONS DURING CENTRAL Si BURNING AND BEYOND FOR
15 M_⊙ AND 25 M_⊙.

Reaction	15 M _⊙			25 M _⊙		
	Int.	Eff.	Flux	Reaction	Int.	Eff.
Convective Si burning						
⁵³ Mn(e ⁻ , ν) ⁵³ Cr	5.87(+16)	0.999		⁵⁵ Fe(e ⁻ , ν) ⁵⁵ Mn	9.34(+16)	0.999
⁵⁵ Fe(e ⁻ , ν) ⁵⁵ Mn	4.36(+16)	0.998		⁵³ Mn(e ⁻ , ν) ⁵³ Cr	7.63(+16)	0.999
³³ S(e ⁻ , ν) ³³ P	1.15(+16)	0.999		⁵⁴ Fe(e ⁻ , ν) ⁵⁴ Mn	5.08(+16)	0.999
⁵⁴ Mn(e ⁻ , ν) ⁵⁴ Cr	9.29(+15)	0.998		⁵⁵ Co(e ⁻ , ν) ⁵⁵ Fe	2.78(+16)	0.999
⁵¹ Cr(e ⁻ , ν) ⁵¹ V	7.68(+15)	0.999		⁵⁶ Co(e ⁻ , ν) ⁵⁶ Fe	2.21(+16)	0.999
⁵⁴ Fe(e ⁻ , ν) ⁵⁴ Mn	7.25(+15)	0.999		⁵⁷ Co(e ⁻ , ν) ⁵⁷ Fe	2.09(+16)	0.999
⁵⁷ Co(e ⁻ , ν) ⁵⁷ Fe	5.18(+15)	0.999		⁵¹ Cr(e ⁻ , ν) ⁵¹ V	7.82(+15)	0.999
³⁵ Cl(e ⁻ , ν) ³⁵ S	3.58(+15)	0.999		⁵⁴ Mn(e ⁻ , ν) ⁵⁴ Cr	5.29(+15)	0.999
³¹ P(e ⁻ , ν) ³¹ Si	2.52(+15)	0.998		³³ S(e ⁻ , ν) ³³ P	3.28(+15)	0.999
³² S(e ⁻ , ν) ³² P	1.53(+15)	0.986		⁵⁹ Ni(e ⁻ , ν) ⁵⁹ Co	3.16(+15)	0.999
⁵⁶ Co(e ⁻ , ν) ⁵⁶ Fe	1.21(+15)	0.999		⁵⁰ Cr(e ⁻ , ν) ⁵⁰ V	2.73(+15)	0.999
⁵⁶ Fe(e ⁻ , ν) ⁵⁶ Mn	1.10(+15)	0.989		³⁵ Cl(e ⁻ , ν) ³⁵ S	2.61(+15)	0.999
⁵⁰ Cr(e ⁻ , ν) ⁵⁰ V	9.50(+14)	0.999		⁵⁸ Ni(e ⁻ , ν) ⁵⁸ Co	1.90(+15)	0.999
⁵² Cr(e ⁻ , ν) ⁵² V	8.81(+14)	0.989		⁵³ Fe(e ⁻ , ν) ⁵³ Mn	1.85(+15)	0.999
⁵⁸ Co(e ⁻ , ν) ⁵⁸ Fe	6.14(+14)	0.999		³² S(e ⁻ , ν) ³² P	1.55(+15)	0.998
⁴⁹ V(e ⁻ , ν) ⁴⁹ Ti	6.13(+14)	0.999		⁵² Mn(e ⁻ , ν) ⁵² Cr	1.43(+15)	0.999
³⁰ P(e ⁻ , ν) ³⁰ Si	6.02(+14)	0.999		⁵⁸ Co(e ⁻ , ν) ⁵⁸ Fe	1.11(+15)	0.999
³⁷ Ar(e ⁻ , ν) ³⁷ Cl	5.18(+14)	0.999		⁵⁶ Fe(e ⁻ , ν) ⁵⁶ Mn	7.71(+14)	0.996
³¹ P(α, p) ³⁰ Si ^a	1.24(+20)	3.84(-4)		⁵⁶ Fe(n, γ) ⁵⁷ Fe ^a	1.97(+20)	1.91(-4)
From Si exhaustion up to NSE						
⁵³ Mn(e ⁻ , ν) ⁵³ Cr	6.82(+16)	0.997		⁵⁵ Fe(e ⁻ , ν) ⁵⁵ Mn	1.33(+15)	0.933
⁵⁵ Fe(e ⁻ , ν) ⁵⁵ Mn	5.61(+16)	0.990		⁵³ Mn(e ⁻ , ν) ⁵³ Cr	8.19(+14)	0.975
⁵⁴ Mn(e ⁻ , ν) ⁵⁴ Cr	1.29(+16)	0.979		⁵⁴ Mn(e ⁻ , ν) ⁵⁴ Cr	5.90(+14)	0.935
⁵⁴ Fe(e ⁻ , ν) ⁵⁴ Mn	9.20(+15)	0.999		⁵⁷ Co(e ⁻ , ν) ⁵⁷ Fe	3.88(+14)	0.968
⁵¹ Cr(e ⁻ , ν) ⁵¹ V	8.96(+15)	0.999		⁵⁸ Co(e ⁻ , ν) ⁵⁸ Fe	2.31(+14)	0.984
⁵⁷ Co(e ⁻ , ν) ⁵⁷ Fe	8.24(+15)	0.996		⁵⁴ Fe(e ⁻ , ν) ⁵⁴ Mn	1.17(+14)	0.989
⁵⁶ Co(e ⁻ , ν) ⁵⁶ Fe	1.99(+15)	0.999		⁵⁶ Co(e ⁻ , ν) ⁵⁶ Fe	8.29(+13)	0.999
⁵⁸ Co(e ⁻ , ν) ⁵⁸ Fe	1.47(+15)	0.994		⁵⁹ Ni(e ⁻ , ν) ⁵⁹ Co	7.63(+13)	0.997
⁵⁶ Fe(e ⁻ , ν) ⁵⁶ Mn	1.30(+15)	0.830		⁵¹ Cr(e ⁻ , ν) ⁵¹ V	7.57(+13)	0.999
³³ S(e ⁻ , ν) ³³ P	1.12(+15)	0.999		⁵⁶ Fe(e ⁻ , ν) ⁵⁶ Mn	6.49(+13)	0.579
⁵⁰ Cr(e ⁻ , ν) ⁵⁰ V	9.44(+14)	0.999		⁵⁵ Co(e ⁻ , ν) ⁵⁵ Fe	2.17(+13)	0.999
⁵⁹ Ni(e ⁻ , ν) ⁵⁹ Co	7.51(+14)	0.999		⁵² Cr(e ⁻ , ν) ⁵² V	1.05(+13)	0.561
⁵⁵ Co(e ⁻ , ν) ⁵⁵ Fe	6.72(+14)	0.999				
⁵² Cr(e ⁻ , ν) ⁵² V	6.36(+14)	0.850				
³⁵ Cl(e ⁻ , ν) ³⁵ S	6.06(+14)	0.999				
⁵² Cr(n, γ) ⁵³ Cr ^a	1.27(+20)	2.84(-5)		⁵⁷ Co(γ, p) ⁵⁶ Fe ^a	1.90(+20)	4.85(-4)
From NSE to collapse						
⁵⁴ Mn(e ⁻ , ν) ⁵⁴ Cr	4.60(+19)	0.855		⁵⁵ Fe(e ⁻ , ν) ⁵⁵ Mn	4.12(+19)	0.869
⁶⁰ Co(e ⁻ , ν) ⁶⁰ Fe	3.92(+19)	0.809		⁵⁴ Mn(e ⁻ , ν) ⁵⁴ Cr	2.65(+19)	0.867

TABLE 8—*Continued*

15 M _⊙			25 M _⊙					
Reaction	Int.	Eff.	Flux	Reaction	Int.	Eff.	Flux	φ
⁵⁸ Co(e ⁻ , ν) ⁵⁸ Fe	3.45(+19)		0.961	⁵⁸ Co(e ⁻ , ν) ⁵⁸ Fe	2.40(+19)		0.964	
⁵⁵ Fe(e ⁻ , ν) ⁵⁵ Mn	3.16(+19)		0.845	⁵³ Mn(e ⁻ , ν) ⁵³ Cr	1.76(+19)		0.935	
⁵³ Mn(e ⁻ , ν) ⁵³ Cr	1.49(+19)		0.934	⁵⁷ Co(e ⁻ , ν) ⁵⁷ Fe	1.59(+19)		0.929	
⁵⁹ Fe(β ⁻ , ν) ⁵⁹ Co	1.12(+19)		0.228	⁶⁰ Co(e ⁻ , ν) ⁶⁰ Fe	5.75(+18)		0.819	
⁵⁷ Co(e ⁻ , ν) ⁵⁷ Fe	1.10(+19)		0.923	⁵⁶ Fe(e ⁻ , ν) ⁵⁶ Mn	5.10(+18)		0.470	
⁵⁷ Mn(β ⁻ , ν) ⁵⁷ Fe	5.83(+18)		0.305	⁵⁹ Ni(e ⁻ , ν) ⁵⁹ Co	4.14(+18)		0.990	
⁵⁶ Fe(e ⁻ , ν) ⁵⁶ Mn	5.27(+18)		0.231	⁵¹ Cr(e ⁻ , ν) ⁵¹ V	1.21(+18)		0.997	
⁵⁹ Ni(e ⁻ , ν) ⁵⁹ Co	2.29(+18)		0.992	⁵⁶ Co(e ⁻ , ν) ⁵⁶ Fe	1.06(+18)		0.998	
⁶⁰ Co(β ⁻ , ν) ⁶⁰ Ni	1.71(+18)		0.260	⁵⁷ Mn(e ⁻ , ν) ⁵⁷ Fe	9.35(+17)		0.227	
⁵⁵ Cr(β ⁻ , ν) ⁵⁵ Mn	1.04(+18)		0.171	⁵⁴ Fe(e ⁻ , ν) ⁵⁴ Mn	8.58(+17)		0.958	
⁵¹ Cr(e ⁻ , ν) ⁵¹ V	7.92(+17)		0.998	⁵² Cr(e ⁻ , ν) ⁵² V	3.93(+17)		0.369	
⁵² Cr(e ⁻ , ν) ⁵² V	3.73(+17)		0.170	⁵⁹ Co(e ⁻ , ν) ⁵⁹ Fe	3.06(+17)		0.031	
⁵⁰ V(e ⁻ , ν) ⁵⁰ Ti	2.33(+17)		0.998	⁶⁰ Co(e ⁻ , ν) ⁶⁰ Ni	2.35(+17)		0.067	
⁵⁴ Fe(e ⁻ , ν) ⁵⁴ Mn	2.04(+17)		0.950	⁵⁰ V(e ⁻ , ν) ⁵⁰ Ti	1.83(+17)		0.997	
⁵⁶ Co(e ⁻ , ν) ⁵⁶ Fe	1.75(+17)		0.999	⁵⁸ Ni(e ⁻ , ν) ⁵⁸ Co	9.90(+16)		0.919	
⁵¹ V(e ⁻ , ν) ⁵¹ Ti	1.05(+17)		0.350	p(e ⁻ , ν)n	6.93(+16)		0.995	
⁴⁹ V(e ⁻ , ν) ⁴⁹ Ti	3.07(+16)		0.994					
⁵⁸ Ni(e ⁻ , ν) ⁵⁸ Co	1.47(+16)		0.888					
⁴⁹ Ti(e ⁻ , ν) ⁴⁹ Sc	8.37(+15)		0.868					
p(e ⁻ , ν)n	8.11(+15)		0.997					

^aNuclear reaction having the maximum integrated flux

TABLE 9
KEY ZONES WHICH KEEP TRACK OF THE VARIOUS NUCLEAR
BURNINGS FOR $13 M_{\odot}$, $15 M_{\odot}$, $20 M_{\odot}$ AND $25 M_{\odot}$ MODELS.

Nuclear burning	$13 M_{\odot}$	$15 M_{\odot}$	$20 M_{\odot}$	$25 M_{\odot}$
Hydrogen (Central)	13.000	15.000	20.000	25.000
Hydrogen (Shell)	3.477	4.282	6.152	8.269
Helium (Shell)	3.066	3.520	5.585	7.638
Helium (Central)	1.751	2.323	3.630	5.190
Carbon	1.749	2.174	2.850	4.560
Neon	1.503	1.754	2.370	2.937
Oxygen	1.390	1.643	2.144	2.113
Silicon	1.290	1.429	1.551	1.569
NSE	0.740	1.080	1.105	1.370
	0.000	0.000	0.000	0.000

TABLE 10
PRESUPERNOVA NUCLEOSYNTHESIS OF THE $13 M_{\odot}$ MODEL

Isotope	Si	O	Ne	C	He _c	He _{sh}	H _{sh}	H _c	Yield (M_{\odot})
1H	0	0	0	0	0	0	0	99	6.11(+00)
2H	0	0	0	0	0	0	0	99	1.74(-16)
3H	0	0	0	0	0	0	99	0	2.60(-40)
3He	0	0	0	0	0	0	0	99	2.07(-04)
4He	0	0	0	0	0	23	8	68	4.56(+00)
6Li	0	0	0	0	0	0	0	99	1.11(-09)
7Li	0	0	0	0	0	0	0	99	1.62(-10)
7Be	0	0	0	0	0	0	99	0	3.68(-26)
9Be	0	0	0	0	0	0	0	99	2.85(-10)
^{10}Be	0	0	0	0	0	0	0	99	1.21(-39)
^{10}B	0	0	0	0	0	0	0	99	1.84(-09)
^{11}B	0	0	0	0	0	0	0	99	1.35(-08)
^{12}C	0	0	0	1	0	82	0	14	1.38(-01)
^{13}C	0	0	0	0	0	0	2	97	1.21(-03)
^{14}C	0	0	0	0	0	99	0	0	8.22(-07)
^{13}N	4	0	0	95	0	0	0	0	2.81(-16)
^{14}N	0	0	0	0	0	2	13	83	3.96(-02)
^{15}N	0	0	0	0	0	2	1	96	1.77(-05)
^{16}N	63	0	0	36	0	0	0	0	2.74(-22)
^{15}O	1	12	2	83	0	0	0	0	1.87(-14)
^{16}O	0	1	20	35	0	22	0	19	4.20(-01)
^{17}O	0	0	0	0	0	0	0	99	1.11(-04)
^{18}O	0	0	0	0	0	82	0	17	8.19(-04)
^{19}O	0	0	0	99	0	0	0	0	6.74(-18)
^{17}F	49	46	3	1	0	0	0	0	4.03(-17)
^{18}F	0	0	0	99	0	0	0	0	9.23(-12)
^{19}F	0	0	0	0	0	52	0	47	6.77(-06)
^{20}F	0	0	0	99	0	0	0	0	6.09(-15)
^{20}Ne	0	0	0	76	0	3	0	18	8.51(-02)
^{21}Ne	0	0	0	50	0	43	0	6	5.67(-04)
^{22}Ne	0	0	0	0	0	94	0	4	2.45(-02)
^{23}Ne	0	0	0	99	0	0	0	0	8.99(-11)
^{21}Na	0	0	0	99	0	0	0	0	5.33(-13)
^{22}Na	0	0	0	99	0	0	0	0	6.60(-07)
^{23}Na	0	0	0	73	0	8	2	16	3.30(-03)
^{24}Na	0	0	0	99	0	0	0	0	2.44(-07)
^{23}Mg	2	0	0	97	0	0	0	0	2.23(-10)
^{24}Mg	0	0	33	45	0	2	0	17	2.87(-02)
^{25}Mg	0	0	4	66	0	18	0	9	6.03(-03)
^{26}Mg	0	0	6	50	0	21	1	19	4.21(-03)
^{27}Mg	0	0	8	91	0	0	0	0	1.87(-08)
^{25}Al	3	2	4	90	0	0	0	0	5.83(-14)
^{26}Al	0	0	17	82	0	0	0	0	5.41(-07)
^{27}Al	0	0	18	57	0	2	0	20	2.79(-03)
^{28}Al	0	0	33	66	0	0	0	0	7.67(-07)
^{27}Si	0	1	31	66	0	0	0	0	1.50(-09)
^{28}Si	6	64	14	2	0	1	0	9	6.53(-02)
^{29}Si	0	3	72	9	0	3	0	10	3.08(-03)

TABLE 10—*Continued*

Isotope	Si	O	Ne	C	He _c	He _{sh}	H _{sh}	H _c	Yield (M _⊙)
³⁰ Si	7	4	66	5	0	4	0	11	2.05(-03)
³¹ Si	3	0	29	67	0	0	0	0	5.70(-07)
³² Si	3	0	74	22	0	0	0	0	1.66(-07)
²⁹ P	89	10	0	0	0	0	0	0	2.49(-11)
³⁰ P	6	8	61	23	0	0	0	0	8.41(-08)
³¹ P	3	7	68	4	0	4	0	10	7.49(-04)
³² P	2	0	87	9	0	0	0	0	2.56(-06)
³³ P	3	11	83	2	0	0	0	0	3.78(-06)
³⁴ P	55	0	35	9	0	0	0	0	4.75(-11)
³¹ S	0	6	93	0	0	0	0	0	4.32(-08)
³² S	2	79	4	0	0	1	0	11	3.41(-02)
³³ S	4	61	15	0	0	4	0	11	2.72(-04)
³⁴ S	12	82	1	0	0	0	0	2	7.91(-03)
³⁵ S	9	0	50	26	0	12	0	0	1.92(-06)
³⁶ S	6	0	31	17	0	26	0	16	5.51(-06)
³⁷ S	92	0	0	7	0	0	0	0	5.90(-13)
³³ Cl	80	19	0	0	0	0	0	0	1.59(-12)
³⁴ Cl	38	58	3	0	0	0	0	0	1.45(-09)
³⁵ Cl	8	60	2	1	0	4	0	21	1.13(-04)
³⁶ Cl	9	30	26	8	0	24	0	0	9.16(-07)
³⁷ Cl	1	5	11	21	0	35	0	22	3.70(-05)
³⁸ Cl	3	0	1	95	0	0	0	0	1.41(-09)
³⁶ Ar	0	78	0	0	0	1	0	17	4.40(-03)
³⁷ Ar	7	83	1	0	0	7	0	0	1.41(-05)
³⁸ Ar	4	93	0	0	0	0	0	1	1.02(-02)
³⁹ Ar	1	0	0	35	0	62	0	0	2.26(-06)
⁴⁰ Ar	1	0	19	21	0	41	0	15	1.56(-06)
⁴¹ Ar	11	0	3	84	0	0	0	0	1.65(-10)
³⁷ K	74	25	0	0	0	0	0	0	2.04(-14)
³⁸ K	31	68	0	0	0	0	0	0	2.13(-10)
³⁹ K	2	70	0	0	0	2	0	22	1.52(-04)
⁴⁰ K	1	1	5	23	0	58	0	9	6.00(-07)
⁴¹ K	0	0	4	7	0	16	2	67	3.79(-06)
⁴² K	2	0	27	69	0	0	0	0	5.65(-09)
⁴⁰ Ca	0	75	0	0	0	2	0	20	2.88(-03)
⁴¹ Ca	0	80	0	2	0	15	0	0	1.07(-05)
⁴² Ca	2	93	0	0	0	1	0	2	1.95(-04)
⁴³ Ca	3	7	4	13	0	23	1	46	1.90(-06)
⁴⁴ Ca	5	0	2	4	0	12	3	71	1.95(-05)
⁴⁵ Ca	18	0	16	30	0	35	0	0	2.50(-07)
⁴⁶ Ca	36	0	18	9	0	31	0	4	5.77(-07)
⁴⁷ Ca	81	0	13	4	0	0	0	0	5.89(-09)
⁴⁸ Ca	0	0	0	1	0	11	3	81	1.65(-06)
⁴⁹ Ca	60	0	0	39	0	0	0	0	2.48(-13)
⁴¹ Sc	76	23	0	0	0	0	0	0	6.46(-16)
⁴² Sc	44	54	0	1	0	0	0	0	1.68(-13)
⁴³ Sc	16	83	0	0	0	0	0	0	4.13(-09)
⁴⁴ Sc	25	69	4	0	0	0	0	0	2.45(-09)

TABLE 10—Continued

TABLE 10—*Continued*

Isotope	Si	O	Ne	C	He _c	He _{sh}	H _{sh}	H _c	Yield (M _⊙)
⁵⁷ Co	99	0	0	0	0	0	0	0	1.62(-03)
⁵⁸ Co	99	0	0	0	0	0	0	0	3.64(-04)
⁵⁹ Co	94	0	0	1	0	2	0	1	1.92(-03)
⁶⁰ Co	98	0	0	0	0	0	0	0	4.26(-05)
⁶¹ Co	99	0	0	0	0	0	0	0	1.37(-05)
⁵⁶ Ni	99	0	0	0	0	0	0	0	2.27(-08)
⁵⁷ Ni	99	0	0	0	0	0	0	0	3.64(-07)
⁵⁸ Ni	37	0	0	0	0	4	2	55	8.73(-04)
⁵⁹ Ni	95	0	0	0	0	4	0	0	1.69(-04)
⁶⁰ Ni	94	1	0	0	0	0	0	2	6.51(-03)
⁶¹ Ni	94	0	0	1	0	2	0	1	6.60(-04)
⁶² Ni	95	0	1	0	0	1	0	1	2.50(-03)
⁶³ Ni	50	0	0	25	0	23	0	0	4.98(-05)
⁶⁴ Ni	12	0	25	19	0	31	0	10	6.71(-05)
⁶⁵ Ni	40	0	0	58	0	0	0	0	3.52(-08)
⁵⁷ Cu	99	0	0	0	0	0	0	0	4.06(-18)
⁵⁸ Cu	99	0	0	0	0	0	0	0	2.34(-14)
⁵⁹ Cu	99	0	0	0	0	0	0	0	2.96(-10)
⁶⁰ Cu	99	0	0	0	0	0	0	0	3.99(-09)
⁶¹ Cu	99	0	0	0	0	0	0	0	8.88(-07)
⁶² Cu	99	0	0	0	0	0	0	0	9.79(-07)
⁶³ Cu	64	0	0	0	0	6	1	27	2.06(-05)
⁶⁴ Cu	99	0	0	0	0	0	0	0	1.19(-06)
⁶⁵ Cu	15	0	3	20	0	34	1	25	1.02(-05)
⁶⁶ Cu	74	0	0	24	0	0	0	0	2.39(-08)
⁶⁴ Zn	3	0	0	3	0	14	3	75	1.29(-05)
⁶⁵ Zn	23	0	1	22	0	53	0	0	6.02(-07)
⁶⁶ Zn	7	0	7	17	0	30	1	34	1.64(-05)
⁶⁷ Zn	1	0	0	23	0	40	1	32	2.60(-06)
⁶⁸ Zn	0	0	17	18	0	27	1	34	3.41(-05)

TABLE 11
PRESUPERNOVA NUCLEOSYNTHESIS OF THE $15 M_{\odot}$ MODEL

Isotope	Si	O	Ne	C	He _c	He _{sh}	H _{sh}	H _c	Yield (M_{\odot})
1H	0	0	0	0	0	0	0	99	6.77(+00)
2H	0	0	0	0	0	0	0	99	1.84(-16)
3H	0	0	0	0	0	0	99	0	3.17(-33)
3He	0	0	0	0	0	0	0	99	2.18(-04)
4He	0	0	0	0	0	18	13	68	5.26(+00)
6Li	0	0	0	0	0	0	0	99	1.26(-17)
7Li	0	0	0	0	0	0	0	99	1.53(-10)
7Be	0	0	0	0	0	0	100	0	1.10(-19)
9Be	0	0	0	0	0	0	0	100	5.03(-11)
^{10}Be	0	0	0	0	0	0	0	99	6.53(-37)
^{10}B	0	0	0	0	0	0	0	100	1.27(-09)
^{11}B	0	0	0	0	0	0	0	100	1.51(-08)
^{12}C	0	0	0	1	17	67	0	13	1.77(-01)
^{13}C	0	0	0	0	0	0	0	99	2.49(-04)
^{14}C	0	0	0	4	0	95	0	0	3.34(-07)
^{13}N	81	2	0	0	15	0	0	0	7.59(-14)
^{14}N	0	0	0	0	0	0	19	80	5.08(-02)
^{15}N	0	0	0	0	0	1	1	97	1.98(-05)
^{16}N	98	0	1	0	0	0	0	0	1.23(-20)
^{15}O	35	62	0	1	0	0	0	0	1.06(-12)
^{16}O	0	3	11	41	17	13	0	12	7.07(-01)
^{17}O	0	0	0	0	0	0	1	98	1.03(-04)
^{18}O	0	0	0	0	0	92	0	7	2.26(-03)
^{19}O	0	0	78	21	0	0	0	0	1.33(-17)
^{17}F	54	45	0	0	0	0	0	0	6.31(-14)
^{18}F	0	0	29	70	0	0	0	0	3.64(-11)
^{19}F	0	0	0	0	0	27	0	71	4.87(-06)
^{20}F	0	0	77	22	0	0	0	0	4.49(-15)
^{20}Ne	0	0	9	73	0	2	0	14	1.25(-01)
^{21}Ne	0	0	4	76	3	10	0	4	8.67(-04)
^{22}Ne	0	0	0	2	9	82	0	4	2.62(-02)
^{23}Ne	0	0	67	32	0	0	0	0	1.28(-10)
^{21}Na	2	0	7	89	0	0	0	0	5.29(-13)
^{22}Na	0	0	4	95	0	0	0	0	6.04(-07)
^{23}Na	0	0	6	75	0	4	2	11	5.60(-03)
^{24}Na	0	0	80	19	0	0	0	0	3.70(-07)
^{23}Mg	4	37	20	38	0	0	0	0	3.85(-10)
^{24}Mg	0	2	26	46	0	2	1	20	2.72(-02)
^{25}Mg	0	0	14	67	4	6	0	7	8.60(-03)
^{26}Mg	0	0	14	48	7	11	1	16	6.01(-03)
^{27}Mg	0	0	97	2	0	0	0	0	1.84(-08)
^{25}Al	81	17	0	0	0	0	0	0	4.32(-12)
^{26}Al	0	0	8	0	0	6	77	5	4.34(-06)
^{27}Al	0	1	16	62	0	1	1	16	3.82(-03)
^{28}Al	0	0	97	1	0	0	0	0	4.70(-07)
^{27}Si	4	72	22	1	0	0	0	0	3.42(-09)
^{28}Si	5	83	2	1	0	0	0	6	1.17(-01)
^{29}Si	0	12	46	13	1	3	1	21	1.74(-03)

TABLE 11—Continued

TABLE 11—Continued

TABLE 11—*Continued*

Isotope	Si	O	Ne	C	He _c	He _{sh}	H _{sh}	H _c	Yield (M _⊙)
⁵⁷ Co	99	0	0	0	0	0	0	0	1.19(-02)
⁵⁸ Co	99	0	0	0	0	0	0	0	5.54(-04)
⁵⁹ Co	48	0	4	20	6	6	0	12	2.93(-04)
⁶⁰ Co	49	0	46	3	0	0	0	0	1.46(-06)
⁶¹ Co	35	0	64	0	0	0	0	0	4.70(-08)
⁵⁶ Ni	97	2	0	0	0	0	0	0	1.48(-03)
⁵⁷ Ni	99	0	0	0	0	0	0	0	1.92(-03)
⁵⁸ Ni	97	0	0	0	0	0	0	1	3.14(-02)
⁵⁹ Ni	99	0	0	0	0	0	0	0	3.85(-03)
⁶⁰ Ni	91	1	0	1	0	0	0	3	5.56(-03)
⁶¹ Ni	67	0	3	13	3	5	0	5	1.67(-04)
⁶² Ni	12	2	15	30	5	10	1	20	1.46(-04)
⁶³ Ni	0	0	15	69	0	13	0	0	4.98(-05)
⁶⁴ Ni	0	2	22	47	3	14	0	9	8.54(-05)
⁶⁵ Ni	0	0	92	7	0	0	0	0	7.79(-08)
⁵⁷ Cu	99	0	0	0	0	0	0	0	5.15(-10)
⁵⁸ Cu	99	0	0	0	0	0	0	0	6.80(-08)
⁵⁹ Cu	99	0	0	0	0	0	0	0	1.36(-05)
⁶⁰ Cu	99	0	0	0	0	0	0	0	1.40(-05)
⁶¹ Cu	99	0	0	0	0	0	0	0	8.90(-05)
⁶² Cu	99	0	0	0	0	0	0	0	1.07(-05)
⁶³ Cu	37	0	0	4	14	4	2	36	1.72(-05)
⁶⁴ Cu	92	0	5	1	0	1	0	0	1.04(-07)
⁶⁵ Cu	0	0	9	49	3	14	1	21	1.38(-05)
⁶⁶ Cu	0	0	95	4	0	0	0	0	1.32(-08)
⁶⁴ Zn	24	0	0	8	8	6	3	47	2.28(-05)
⁶⁵ Zn	18	0	3	37	25	15	0	0	1.39(-06)
⁶⁶ Zn	0	0	10	39	7	13	1	25	2.48(-05)
⁶⁷ Zn	0	0	10	45	7	14	1	20	4.73(-06)
⁶⁸ Zn	0	1	16	39	3	12	1	23	5.59(-05)

TABLE 12
PRESUPERNOVA NUCLEOSYNTHESIS OF THE $20 M_{\odot}$ MODEL

Isotope	Si	O	Ne	C	He _c	He _{sh}	H _{sh}	H _c	Yield (M_{\odot})
¹ H	0	0	0	0	0	0	0	99	8.34(+00)
² H	0	0	0	0	0	0	0	99	2.02(-16)
³ H	0	0	0	0	0	0	98	1	3.61(-33)
³ He	0	0	0	0	0	0	0	99	2.32(-04)
⁴ He	0	0	0	0	0	23	6	70	7.18(+00)
⁶ Li	0	0	0	0	0	0	0	99	2.33(-17)
⁷ Li	0	0	0	0	0	0	0	99	1.31(-10)
⁷ Be	0	0	0	0	0	0	100	0	5.09(-17)
⁹ Be	0	0	0	0	0	0	0	100	5.75(-11)
¹⁰ Be	0	0	0	0	0	0	0	99	1.19(-36)
¹⁰ B	0	0	0	0	0	0	0	100	1.54(-09)
¹¹ B	0	0	0	0	0	0	0	100	1.87(-08)
¹² C	0	0	0	10	36	45	0	7	3.78(-01)
¹³ C	0	0	0	0	0	0	0	99	3.05(-04)
¹⁴ C	0	0	0	33	0	65	0	0	2.47(-07)
¹³ N	1	0	0	21	77	0	0	0	9.47(-12)
¹⁴ N	0	0	0	0	0	0	9	89	7.30(-02)
¹⁵ N	0	0	0	0	0	1	0	97	2.49(-05)
¹⁶ N	99	0	0	0	0	0	0	0	1.24(-17)
¹⁵ O	0	25	0	73	0	0	0	0	2.17(-11)
¹⁶ O	0	10	11	24	42	5	0	6	1.52(+00)
¹⁷ O	0	0	0	0	0	0	0	99	1.14(-04)
¹⁸ O	0	0	0	0	0	82	0	17	1.02(-03)
¹⁹ O	0	0	16	83	0	0	0	0	4.14(-16)
¹⁷ F	11	88	0	0	0	0	0	0	2.18(-13)
¹⁸ F	0	0	1	98	0	0	0	0	2.04(-09)
¹⁹ F	0	0	0	0	0	46	0	52	6.84(-06)
²⁰ F	0	0	1	98	0	0	0	0	4.02(-12)
²⁰ Ne	0	0	24	48	2	2	0	20	1.11(-01)
²¹ Ne	0	0	12	54	19	10	0	3	1.05(-03)
²² Ne	0	0	0	5	19	71	0	2	5.37(-02)
²³ Ne	0	0	5	94	0	0	0	0	1.81(-08)
²¹ Na	0	0	0	96	3	0	0	0	5.97(-11)
²² Na	0	0	3	93	2	0	0	0	2.30(-06)
²³ Na	0	0	15	57	3	6	1	16	5.74(-03)
²⁴ Na	0	0	16	83	0	0	0	0	1.47(-05)
²³ Mg	0	0	4	94	0	0	0	0	5.28(-08)
²⁴ Mg	0	10	40	18	1	3	0	24	2.99(-02)
²⁵ Mg	0	0	21	37	31	3	0	6	1.12(-02)
²⁶ Mg	0	0	17	25	36	5	0	13	1.03(-02)
²⁷ Mg	0	0	64	35	0	0	0	0	1.43(-07)
²⁵ Al	31	18	0	30	18	0	0	0	5.79(-12)
²⁶ Al	0	0	8	16	0	3	21	48	2.28(-05)
²⁷ Al	0	2	32	40	1	2	0	20	4.00(-03)
²⁸ Al	0	0	77	22	0	0	0	0	4.42(-06)
²⁷ Si	0	40	42	17	0	0	0	0	3.13(-08)
²⁸ Si	1	91	1	0	0	0	0	3	2.42(-01)
²⁹ Si	0	25	44	4	4	3	0	17	2.85(-03)

TABLE 12—Continued

TABLE 12—Continued

TABLE 12—*Continued*

Isotope	Si	O	Ne	C	He _c	He _{sh}	H _{sh}	H _c	Yield (M _⊙)
⁵⁷ Co	99	0	0	0	0	0	0	0	1.63(-02)
⁵⁸ Co	99	0	0	0	0	0	0	0	2.21(-03)
⁵⁹ Co	88	0	0	2	5	0	0	2	2.33(-03)
⁶⁰ Co	89	0	4	6	0	0	0	0	1.26(-04)
⁶¹ Co	74	0	19	5	0	0	0	0	1.58(-05)
⁵⁶ Ni	97	2	0	0	0	0	0	0	4.16(-04)
⁵⁷ Ni	99	0	0	0	0	0	0	0	9.02(-04)
⁵⁸ Ni	95	1	0	0	0	0	0	2	2.42(-02)
⁵⁹ Ni	99	0	0	0	0	0	0	0	4.57(-03)
⁶⁰ Ni	92	3	0	0	0	0	0	2	1.33(-02)
⁶¹ Ni	93	0	0	1	2	0	0	0	1.68(-03)
⁶² Ni	75	3	3	5	7	0	0	3	1.19(-03)
⁶³ Ni	32	0	23	36	4	2	0	0	9.94(-05)
⁶⁴ Ni	1	3	32	29	25	1	0	5	1.78(-04)
⁶⁵ Ni	1	0	27	70	0	0	0	0	2.19(-06)
⁵⁷ Cu	99	0	0	0	0	0	0	0	5.14(-11)
⁵⁸ Cu	99	0	0	0	0	0	0	0	1.36(-08)
⁵⁹ Cu	99	0	0	0	0	0	0	0	4.61(-06)
⁶⁰ Cu	99	0	0	0	0	0	0	0	9.23(-06)
⁶¹ Cu	99	0	0	0	0	0	0	0	8.93(-05)
⁶² Cu	99	0	0	0	0	0	0	0	2.75(-05)
⁶³ Cu	58	0	0	5	26	0	0	7	1.13(-04)
⁶⁴ Cu	83	0	1	13	1	0	0	0	9.91(-06)
⁶⁵ Cu	9	1	9	31	32	2	0	12	3.02(-05)
⁶⁶ Cu	37	0	24	38	0	0	0	0	2.42(-07)
⁶⁴ Zn	18	0	1	13	40	3	0	21	6.52(-05)
⁶⁵ Zn	26	0	2	21	46	2	0	0	1.07(-05)
⁶⁶ Zn	5	4	10	28	38	2	0	10	8.20(-05)
⁶⁷ Zn	1	0	12	33	42	2	0	7	1.57(-05)
⁶⁸ Zn	0	3	26	31	27	1	0	9	1.73(-04)

TABLE 13
PRESUPERNOVA NUCLEOSYNTHESIS OF THE $25 M_{\odot}$ MODEL

Isotope	Si	O	Ne	C	He _c	He _{sh}	H _{sh}	H _c	Yield (M_{\odot})
1H	0	0	0	0	0	0	0	99	9.82(+00)
2H	0	0	0	0	0	0	0	99	2.29(-16)
3H	0	0	0	0	0	0	93	6	3.98(-33)
3He	0	0	0	0	0	0	0	99	2.65(-04)
4He	0	0	0	0	0	23	5	70	8.99(+00)
6Li	0	0	0	0	0	0	0	99	3.67(-17)
7Li	0	0	0	0	0	0	0	99	9.27(-11)
7Be	0	0	0	0	0	0	100	0	2.08(-15)
9Be	0	0	0	0	0	0	0	99	6.36(-11)
^{10}Be	0	0	0	0	0	0	0	99	1.58(-36)
^{10}B	0	0	0	0	0	0	0	99	1.78(-09)
^{11}B	0	0	0	0	0	0	0	99	2.19(-08)
^{12}C	0	0	0	4	31	54	0	8	3.89(-01)
^{13}C	0	0	0	0	0	0	0	99	3.61(-04)
^{14}C	0	0	3	15	0	81	0	0	1.73(-07)
^{13}N	80	19	0	0	0	0	0	0	1.17(-13)
^{14}N	0	0	0	0	0	0	8	91	9.37(-02)
^{15}N	0	0	0	0	0	1	0	97	2.94(-05)
^{16}N	2	0	92	4	0	0	0	0	4.02(-22)
^{15}O	6	89	4	0	0	0	0	0	5.53(-12)
^{16}O	0	6	23	43	19	2	0	4	2.68(+00)
^{17}O	0	0	0	0	0	0	0	99	1.15(-04)
^{18}O	0	0	0	0	0	83	0	16	1.31(-03)
^{19}O	0	0	99	0	0	0	0	0	8.98(-18)
^{17}F	23	76	0	0	0	0	0	0	2.27(-13)
^{18}F	0	0	88	11	0	0	0	0	1.43(-10)
^{19}F	0	0	0	0	0	44	0	55	7.44(-06)
^{20}F	0	0	99	0	0	0	0	0	1.13(-13)
^{20}Ne	0	0	26	66	0	0	0	5	4.87(-01)
^{21}Ne	0	0	19	67	7	3	0	1	2.38(-03)
^{22}Ne	0	0	0	2	13	80	0	2	6.04(-02)
^{23}Ne	0	0	99	0	0	0	0	0	2.01(-10)
^{21}Na	0	1	63	34	0	0	0	0	1.75(-12)
^{22}Na	0	0	18	81	0	0	0	0	7.15(-06)
^{23}Na	0	0	21	69	0	2	0	5	1.97(-02)
^{24}Na	0	0	78	21	0	0	0	0	5.61(-06)
^{23}Mg	0	1	98	0	0	0	0	0	2.97(-08)
^{24}Mg	0	11	36	41	0	1	0	8	1.05(-01)
^{25}Mg	0	0	27	58	10	1	0	2	3.21(-02)
^{26}Mg	0	1	26	49	13	2	0	6	2.60(-02)
^{27}Mg	0	1	98	0	0	0	0	0	4.81(-07)
^{25}Al	69	29	0	0	0	0	0	0	4.40(-11)
^{26}Al	0	0	25	0	0	1	14	58	3.98(-05)
^{27}Al	0	3	31	58	0	0	0	5	1.80(-02)
^{28}Al	0	7	92	0	0	0	0	0	2.69(-05)
^{27}Si	0	3	96	0	0	0	0	0	1.89(-07)
^{28}Si	12	75	4	2	0	0	0	4	2.50(-01)
^{29}Si	0	30	42	15	1	1	0	7	7.46(-03)

TABLE 13—*Continued*

Isotope	Si	O	Ne	C	He _c	He _{sh}	H _{sh}	H _c	Yield (M _⊙)
³⁰ Si	0	35	34	15	3	1	0	9	4.34(-03)
³¹ Si	0	0	98	0	0	0	0	0	2.48(-05)
³² Si	0	12	60	27	0	0	0	0	1.33(-06)
²⁹ P	57	42	0	0	0	0	0	0	4.69(-07)
³⁰ P	32	40	26	0	0	0	0	0	2.54(-06)
³¹ P	1	36	22	23	5	1	0	8	1.65(-03)
³² P	0	19	45	35	0	0	0	0	1.95(-05)
³³ P	0	36	43	20	0	0	0	0	5.39(-06)
³⁴ P	0	2	97	0	0	0	0	0	7.24(-10)
³¹ S	36	62	1	0	0	0	0	0	2.74(-07)
³² S	9	82	0	0	0	0	0	5	1.22(-01)
³³ S	3	78	3	1	0	2	0	8	6.33(-04)
³⁴ S	0	91	1	0	0	0	0	5	6.38(-03)
³⁵ S	0	1	46	49	0	1	0	0	8.58(-06)
³⁶ S	0	5	27	45	14	1	0	5	2.98(-05)
³⁷ S	0	0	98	0	0	0	0	0	4.03(-13)
³³ Cl	59	40	0	0	0	0	0	0	7.85(-08)
³⁴ Cl	48	51	0	0	0	0	0	0	5.19(-07)
³⁵ Cl	5	80	1	1	0	1	0	8	5.17(-04)
³⁶ Cl	1	42	15	21	11	7	0	0	2.69(-06)
³⁷ Cl	0	3	21	42	20	4	0	8	1.77(-04)
³⁸ Cl	0	0	99	0	0	0	0	0	2.74(-08)
³⁶ Ar	8	83	0	0	0	0	0	6	1.96(-02)
³⁷ Ar	6	91	0	0	0	1	0	0	1.06(-04)
³⁸ Ar	0	92	0	1	0	0	0	3	7.01(-03)
³⁹ Ar	0	0	32	62	1	3	0	0	1.17(-05)
⁴⁰ Ar	0	5	31	47	8	1	0	4	8.75(-06)
⁴¹ Ar	0	0	98	1	0	0	0	0	1.14(-08)
³⁷ K	63	36	0	0	0	0	0	0	2.77(-09)
³⁸ K	47	52	0	0	0	0	0	0	1.70(-07)
³⁹ K	3	84	0	1	0	1	0	7	7.65(-04)
⁴⁰ K	0	3	20	43	19	10	0	2	3.42(-06)
⁴¹ K	0	2	11	22	9	7	1	44	1.01(-05)
⁴² K	0	1	86	12	0	0	0	0	4.52(-07)
⁴⁰ Ca	6	84	0	0	0	1	0	7	1.40(-02)
⁴¹ Ca	6	82	1	2	1	6	0	0	3.46(-05)
⁴² Ca	1	91	1	2	1	0	0	2	2.59(-04)
⁴³ Ca	0	4	15	32	14	5	0	26	5.83(-06)
⁴⁴ Ca	0	1	10	19	6	7	1	51	4.72(-05)
⁴⁵ Ca	0	2	42	52	0	1	0	0	2.56(-06)
⁴⁶ Ca	0	12	38	45	0	0	0	2	1.70(-06)
⁴⁷ Ca	0	5	69	24	0	0	0	0	9.95(-08)
⁴⁸ Ca	0	0	2	5	2	10	2	74	3.18(-06)
⁴⁹ Ca	0	0	99	0	0	0	0	0	5.89(-13)
⁴¹ Sc	68	31	0	0	0	0	0	0	2.36(-10)
⁴² Sc	70	29	0	0	0	0	0	0	6.95(-10)
⁴³ Sc	25	74	0	0	0	0	0	0	3.13(-07)
⁴⁴ Sc	27	70	1	0	0	0	0	0	2.09(-08)

TABLE 13—Continued

TABLE 13—*Continued*

Isotope	Si	O	Ne	C	He _c	He _{sh}	H _{sh}	H _c	Yield (M _⊙)
⁵⁷ Co	98	1	0	0	0	0	0	0	4.01(-03)
⁵⁸ Co	99	0	0	0	0	0	0	0	6.08(-05)
⁵⁹ Co	2	1	15	41	21	3	0	13	4.39(-04)
⁶⁰ Co	0	0	67	32	0	0	0	0	1.90(-05)
⁶¹ Co	0	2	97	0	0	0	0	0	1.02(-05)
⁵⁶ Ni	72	27	0	0	0	0	0	0	7.85(-04)
⁵⁷ Ni	92	7	0	0	0	0	0	0	6.63(-04)
⁵⁸ Ni	87	4	0	0	0	0	0	6	1.34(-02)
⁵⁹ Ni	97	0	0	0	0	1	0	0	8.80(-04)
⁶⁰ Ni	50	9	4	11	5	2	0	15	2.15(-03)
⁶¹ Ni	2	0	20	46	19	3	0	6	2.13(-04)
⁶² Ni	0	17	22	36	13	1	0	7	6.45(-04)
⁶³ Ni	0	0	31	66	1	0	0	0	3.00(-04)
⁶⁴ Ni	0	7	33	48	8	0	0	2	6.00(-04)
⁶⁵ Ni	0	0	94	5	0	0	0	0	1.44(-06)
⁵⁷ Cu	93	6	0	0	0	0	0	0	4.11(-11)
⁵⁸ Cu	97	2	0	0	0	0	0	0	6.39(-09)
⁵⁹ Cu	98	1	0	0	0	0	0	0	2.12(-06)
⁶⁰ Cu	99	0	0	0	0	0	0	0	1.33(-06)
⁶¹ Cu	99	0	0	0	0	0	0	0	1.00(-05)
⁶² Cu	99	0	0	0	0	0	0	0	4.26(-07)
⁶³ Cu	0	0	4	16	56	2	0	19	5.10(-05)
⁶⁴ Cu	0	0	42	55	1	0	0	0	1.09(-06)
⁶⁵ Cu	0	1	21	59	11	0	0	4	9.35(-05)
⁶⁶ Cu	0	0	99	0	0	0	0	0	3.61(-07)
⁶⁴ Zn	0	0	7	26	37	3	0	23	7.12(-05)
⁶⁵ Zn	0	0	13	43	40	2	0	0	1.24(-05)
⁶⁶ Zn	0	7	21	49	16	0	0	4	2.07(-04)
⁶⁷ Zn	0	0	23	55	17	0	0	3	4.24(-05)
⁶⁸ Zn	0	6	30	51	8	0	0	2	6.91(-04)

TABLE 14
 COMPARISON OF THE LAST C CONVECTIVE SHELL EXTENSION
 AMONG NH88, WW95, APB96 AND THE PRESENT
 COMPUTATIONS.

Initial Mass	NH88	WW95	APB96	LCS
13	1.44-1.70	1.52-1.75
15	1.50-2.00	2.00-2.30	...	1.64-2.18
20	1.67-3.70	...	1.40-3.80	2.39-2.77
25	1.79-5.40	3.70-5.60	...	2.28-4.61

TABLE 15
 NUCLEOSYNTHESIS AFTER CENTRAL NE EXHAUSTION FOR ISOTOPES
 LIGHTER THAN $A=27$ IN THE $20 M_{\odot}$ MODEL

Isotope	Ne exh. (A)	Last Model (B)	(A-B)/A	Burning Site
1H	8.34E+00	8.34E+00	0.0000	
2H	2.02E-16	2.02E-16	0.0000	
3He	2.32E-04	2.32E-04	0.0000	
4He	7.19E+00	7.18E+00	0.0014	
6Li	2.33E-17	2.33E-17	0.0000	
7Li	1.31E-10	1.31E-10	0.0000	
9Be	5.75E-11	5.75E-11	0.0000	
^{10}B	1.54E-09	1.54E-09	0.0000	
^{11}B	1.87E-08	1.87E-08	0.0000	
^{12}C	3.91E-01	3.78E-01	0.0332	
^{13}C	3.04E-04	3.05E-04	-0.0033	
^{14}N	7.41E-02	7.30E-02	0.0148	
^{15}N	2.47E-05	2.49E-05	-0.0081	
^{16}O	1.57E+00	1.48E+00	0.0573	
^{17}O	1.14E-04	1.14E-04	0.0000	
^{18}O	4.61E-03	1.02E-03	0.7787	d(He shell)
^{19}F	5.35E-06	6.84E-06	-0.2785	p(He shell)
^{20}Ne	1.74E-01	1.11E-01	0.3621	d(Ne shell)
^{21}Ne	1.71E-03	1.05E-03	0.3860	d(Ne shell)
^{22}Ne	5.03E-02	5.37E-02	-0.0676	p(He shell)
^{23}Na	9.66E-03	5.74E-03	0.4058	d(Ne shell)
^{24}Mg	2.32E-02	2.96E-02	-0.2759	p(Ne shell)
^{25}Mg	1.36E-02	1.12E-02	0.1765	d(Ne shell)
^{26}Mg	1.13E-02	1.03E-02	0.0885	d(O shell)
^{27}Al	4.99E-03	4.00E-03	0.1984	d(Ne shell)

TABLE A1
EXPLOSIVE NUCLEOSYNTHESIS OF THE $13 M_{\odot}$ $Z = 2 \cdot 10^{-2}$ MODEL

	(1)	(2)	(3)	(4)	(5)
$M(^{56}\text{Ni})$	0.001	0.005	0.010	0.050	0.060
M_{ejected}	11.41	11.42	11.43	11.50	11.51
M_{cut}	1.59	1.58	1.57	1.50	1.49
C	1.37(-01)	1.37(-01)	1.37(-01)	1.37(-01)	1.37(-01)
N	3.97(-02)	3.97(-02)	3.97(-02)	3.97(-02)	3.97(-02)
O	2.66(-01)	2.66(-01)	2.66(-01)	2.66(-01)	2.66(-01)
F	6.75(-06)	6.75(-06)	6.75(-06)	6.75(-06)	6.75(-06)
Ne	5.15(-02)	5.15(-02)	5.15(-02)	5.15(-02)	5.15(-02)
Na	1.05(-03)	1.05(-03)	1.05(-03)	1.05(-03)	1.05(-03)
Mg	1.84(-02)	1.84(-02)	1.84(-02)	1.84(-02)	1.84(-02)
Al	9.80(-04)	9.80(-04)	9.80(-04)	9.80(-04)	9.80(-04)
Si	3.97(-02)	4.50(-02)	4.52(-02)	4.52(-02)	4.52(-02)
P	3.21(-04)	3.21(-04)	3.21(-04)	3.21(-04)	3.21(-04)
S	2.01(-02)	2.40(-02)	2.42(-02)	2.42(-02)	2.42(-02)
Cl	8.56(-05)	8.57(-05)	8.57(-05)	8.58(-05)	8.58(-05)
Ar	3.54(-03)	4.37(-03)	4.48(-03)	4.49(-03)	4.50(-03)
K	6.49(-05)	6.50(-05)	6.50(-05)	6.52(-05)	6.53(-05)
Ca	2.19(-03)	3.04(-03)	3.24(-03)	3.33(-03)	3.34(-03)
Sc	7.96(-07)	7.99(-07)	8.00(-07)	8.27(-07)	8.28(-07)
Ti	4.48(-05)	5.97(-05)	6.62(-05)	1.48(-04)	1.65(-04)
V	6.74(-06)	8.61(-06)	9.21(-06)	9.24(-06)	9.24(-06)
Cr	3.30(-04)	5.79(-04)	7.45(-04)	8.70(-04)	8.93(-04)
Mn	2.34(-04)	3.25(-04)	3.83(-04)	3.93(-04)	3.93(-04)
Fe	1.76(-02)	2.25(-02)	2.78(-02)	6.99(-02)	8.04(-02)
Co	9.24(-05)	9.24(-05)	9.24(-05)	1.06(-03)	1.32(-03)
Ni	1.08(-03)	1.15(-03)	1.21(-03)	3.65(-03)	4.15(-03)
Cu	2.93(-05)	2.93(-05)	2.93(-05)	2.93(-05)	2.93(-05)
Zn	5.06(-05)	5.06(-05)	5.06(-05)	5.07(-05)	5.08(-05)

TABLE A2
EXPLOSIVE NUCLEOSYNTHESIS OF THE $13 M_{\odot}$ $Z = 10^{-3}$ MODEL

	(1)	(2)	(3)	(4)	(5)
$M(^{56}\text{Ni})$	0.001	0.005	0.010	0.050	0.063
M_{ejected}	1.65	1.63	1.62	1.56	1.53
M_{cut}	11.35	11.37	11.38	11.44	11.47
C	1.24(-01)	1.24(-01)	1.24(-01)	1.24(-01)	1.24(-01)
N	2.61(-03)	2.61(-03)	2.61(-03)	2.61(-03)	2.61(-03)
O	1.89(-01)	1.89(-01)	1.89(-01)	1.89(-01)	1.89(-01)
F	2.70(-07)	2.70(-07)	2.70(-07)	2.70(-07)	2.70(-07)
Ne	1.05(-02)	1.05(-02)	1.05(-02)	1.05(-02)	1.05(-02)
Na	1.37(-04)	1.37(-04)	1.37(-04)	1.37(-04)	1.37(-04)
Mg	1.57(-02)	1.57(-02)	1.57(-02)	1.57(-02)	1.57(-02)
Al	1.56(-04)	1.56(-04)	1.56(-04)	1.56(-04)	1.56(-04)
Si	3.03(-02)	3.87(-02)	3.98(-02)	3.99(-02)	3.99(-02)
P	6.69(-05)	6.70(-05)	6.71(-05)	6.71(-05)	6.71(-05)
S	1.43(-02)	2.00(-02)	2.11(-02)	2.12(-02)	2.12(-02)
Cl	1.71(-05)	1.71(-05)	1.71(-05)	1.83(-05)	2.39(-05)
Ar	2.39(-03)	3.55(-03)	3.86(-03)	3.92(-03)	3.92(-03)
K	9.31(-06)	9.33(-06)	9.34(-06)	9.34(-06)	9.40(-06)
Ca	1.94(-03)	3.04(-03)	3.47(-03)	3.64(-03)	3.68(-03)
Sc	5.31(-08)	5.49(-08)	5.58(-08)	6.37(-07)	4.79(-06)
Ti	7.76(-06)	2.52(-05)	3.64(-05)	9.34(-05)	1.37(-04)
V	7.42(-07)	1.57(-06)	1.90(-06)	2.02(-06)	2.02(-06)
Cr	8.11(-05)	3.37(-04)	5.60(-04)	7.59(-04)	8.19(-04)
Mn	3.20(-05)	7.31(-05)	9.72(-05)	1.12(-04)	1.12(-04)
Fe	2.08(-03)	6.32(-03)	1.14(-02)	5.25(-02)	6.56(-02)
Co	4.18(-06)	4.18(-06)	4.18(-06)	4.47(-04)	6.81(-04)
Ni	7.66(-05)	1.02(-04)	1.18(-04)	5.52(-04)	1.07(-03)
Cu	8.82(-07)	8.82(-07)	8.82(-07)	8.82(-07)	8.82(-07)
Zn	2.09(-06)	2.09(-06)	2.09(-06)	2.10(-06)	2.14(-06)

TABLE A3
EXPLOSIVE NUCLEOSYNTHESIS OF THE $15 M_{\odot}$ $Z = 2 \cdot 10^{-2}$ MODEL

	(1)	(2)	(3)	(4)	(5)	(6)
$M(^{56}\text{Ni})$	0.001	0.005	0.010	0.050	0.100	0.129
M_{ejected}	13.21	13.24	13.26	13.31	13.38	13.43
M_{cut}	1.79	1.76	1.74	1.69	1.62	1.57
C	1.72(-01)	1.72(-01)	1.72(-01)	1.72(-01)	1.72(-01)	1.72(-01)
N	5.08(-02)	5.08(-02)	5.08(-02)	5.08(-02)	5.08(-02)	5.08(-02)
O	5.51(-01)	5.51(-01)	5.51(-01)	5.51(-01)	5.51(-01)	5.51(-01)
F	4.86(-06)	4.86(-06)	4.86(-06)	4.86(-06)	4.86(-06)	4.86(-06)
Ne	5.97(-02)	5.97(-02)	5.97(-02)	5.97(-02)	5.97(-02)	5.97(-02)
Na	1.59(-03)	1.59(-03)	1.59(-03)	1.59(-03)	1.59(-03)	1.59(-03)
Mg	2.91(-02)	2.91(-02)	2.91(-02)	2.91(-02)	2.91(-02)	2.91(-02)
Al	1.55(-03)	1.55(-03)	1.55(-03)	1.55(-03)	1.55(-03)	1.55(-03)
Si	8.20(-02)	9.49(-02)	9.82(-02)	9.94(-02)	9.94(-02)	9.94(-02)
P	6.66(-04)	6.66(-04)	6.66(-04)	6.66(-04)	6.66(-04)	6.66(-04)
S	4.04(-02)	4.90(-02)	5.18(-02)	5.31(-02)	5.31(-02)	5.31(-02)
Cl	1.42(-04)	1.42(-04)	1.42(-04)	1.43(-04)	1.43(-04)	1.43(-04)
Ar	6.85(-03)	8.51(-03)	9.19(-03)	9.66(-03)	9.67(-03)	9.68(-03)
K	1.07(-04)	1.07(-04)	1.07(-04)	1.07(-04)	1.07(-04)	1.07(-04)
Ca	3.83(-03)	5.32(-03)	6.09(-03)	6.87(-03)	6.93(-03)	6.99(-03)
Sc	1.08(-06)	1.09(-06)	1.09(-06)	1.09(-06)	1.10(-06)	1.10(-06)
Ti	6.00(-05)	8.00(-05)	9.59(-05)	1.36(-04)	2.03(-04)	2.57(-04)
V	9.44(-06)	1.26(-05)	1.43(-05)	1.68(-05)	1.68(-05)	1.68(-05)
Cr	4.17(-04)	7.25(-04)	1.01(-03)	1.71(-03)	1.81(-03)	1.88(-03)
Mn	2.97(-04)	4.27(-04)	5.16(-04)	7.32(-04)	7.32(-04)	7.32(-04)
Fe	2.14(-02)	2.70(-02)	3.27(-02)	7.48(-02)	1.27(-01)	1.58(-01)
Co	1.16(-04)	1.16(-04)	1.16(-04)	2.52(-04)	8.55(-04)	1.57(-03)
Ni	1.46(-03)	1.57(-03)	1.63(-03)	2.93(-03)	5.99(-03)	7.64(-03)
Cu	4.58(-05)	4.58(-05)	4.58(-05)	4.58(-05)	4.58(-05)	4.58(-05)
Zn	7.50(-05)	7.50(-05)	7.50(-05)	7.50(-05)	7.51(-05)	7.52(-05)

TABLE A4
EXPLOSIVE NUCLEOSYNTHESIS OF THE $15 M_{\odot}$ $Z = 10^{-3}$ MODEL

	(1)	(2)	(3)	(4)	(5)	(6)
$M(^{56}\text{Ni})$	0.001	0.005	0.010	0.050	0.100	0.127
M_{ejected}	13.18	13.21	13.23	13.28	13.35	13.39
M_{cut}	1.82	1.79	1.77	1.72	1.65	1.61
C	1.58(-01)	1.58(-01)	1.58(-01)	1.58(-01)	1.58(-01)	1.58(-01)
N	3.16(-03)	3.16(-03)	3.16(-03)	3.16(-03)	3.16(-03)	3.16(-03)
O	3.58(-01)	3.58(-01)	3.58(-01)	3.58(-01)	3.58(-01)	3.58(-01)
F	3.42(-07)	3.42(-07)	3.42(-07)	3.42(-07)	3.42(-07)	3.42(-07)
Ne	1.56(-02)	1.56(-02)	1.56(-02)	1.56(-02)	1.56(-02)	1.56(-02)
Na	2.38(-04)	2.38(-04)	2.38(-04)	2.38(-04)	2.38(-04)	2.38(-04)
Mg	3.23(-02)	3.23(-02)	3.23(-02)	3.23(-02)	3.23(-02)	3.23(-02)
Al	3.46(-04)	3.46(-04)	3.46(-04)	3.46(-04)	3.46(-04)	3.46(-04)
Si	5.69(-02)	7.12(-02)	7.65(-02)	7.80(-02)	7.80(-02)	7.80(-02)
P	1.33(-04)	1.33(-04)	1.33(-04)	1.33(-04)	1.33(-04)	1.33(-04)
S	2.58(-02)	3.51(-02)	3.94(-02)	4.10(-02)	4.10(-02)	4.10(-02)
Cl	3.74(-05)	3.74(-05)	3.75(-05)	3.75(-05)	4.04(-05)	4.35(-05)
Ar	4.11(-03)	5.86(-03)	6.86(-03)	7.38(-03)	7.39(-03)	7.40(-03)
K	1.73(-05)	1.73(-05)	1.73(-05)	1.74(-05)	1.74(-05)	1.74(-05)
Ca	3.15(-03)	4.69(-03)	5.74(-03)	6.54(-03)	6.61(-03)	6.66(-03)
Sc	8.22(-08)	8.46(-08)	8.62(-08)	1.09(-07)	2.07(-06)	4.83(-06)
Ti	9.15(-06)	2.96(-05)	4.89(-05)	8.97(-05)	1.63(-04)	2.09(-04)
V	9.36(-07)	2.04(-06)	2.75(-06)	3.50(-06)	3.50(-06)	3.50(-06)
Cr	8.74(-05)	3.68(-04)	6.70(-04)	1.30(-03)	1.41(-03)	1.47(-03)
Mn	3.80(-05)	8.82(-05)	1.26(-04)	1.90(-04)	1.90(-04)	1.90(-04)
Fe	2.34(-03)	6.67(-03)	1.18(-02)	5.27(-02)	1.04(-01)	1.32(-01)
Co	6.19(-06)	6.19(-06)	6.19(-06)	1.45(-04)	5.64(-04)	9.66(-04)
Ni	9.66(-05)	1.25(-04)	1.44(-04)	3.22(-04)	1.08(-03)	1.70(-03)
Cu	1.10(-06)	1.10(-06)	1.10(-06)	1.10(-06)	1.10(-06)	1.10(-06)
Zn	2.51(-06)	2.51(-06)	2.51(-06)	2.51(-06)	2.53(-06)	2.57(-06)

TABLE A5
EXPLOSIVE NUCLEOSYNTHESIS OF THE $15 M_{\odot}$ $Z = 0$ MODEL

	(1)	(2)	(3)	(4)	(5)
$M(^{56}\text{Ni})$	0.001	0.005	0.010	0.050	0.065
M_{ejected}	13.31	13.34	13.35	13.40	13.43
M_{cut}	1.69	1.66	1.65	1.60	1.57
C	1.05(-01)	1.05(-01)	1.05(-01)	1.05(-01)	1.05(-01)
N	1.12(-02)	1.12(-02)	1.12(-02)	1.12(-02)	1.12(-02)
O	1.63(-01)	1.63(-01)	1.63(-01)	1.63(-01)	1.63(-01)
F	3.00(-11)	3.00(-11)	3.00(-11)	3.00(-11)	3.00(-11)
Ne	3.99(-03)	3.99(-03)	3.99(-03)	3.99(-03)	3.99(-03)
Na	2.64(-05)	2.64(-05)	2.64(-05)	2.64(-05)	2.64(-05)
Mg	1.36(-02)	1.36(-02)	1.36(-02)	1.36(-02)	1.36(-02)
Al	5.23(-05)	5.23(-05)	5.23(-05)	5.23(-05)	5.23(-05)
Si	2.74(-02)	3.67(-02)	3.87(-02)	3.88(-02)	3.88(-02)
P	2.42(-05)	2.44(-05)	2.45(-05)	2.46(-05)	2.47(-05)
S	1.38(-02)	2.02(-02)	2.19(-02)	2.21(-02)	2.21(-02)
Cl	9.58(-06)	9.62(-06)	9.63(-06)	1.27(-05)	2.03(-05)
Ar	2.48(-03)	3.73(-03)	4.19(-03)	4.27(-03)	4.27(-03)
K	4.19(-06)	4.20(-06)	4.21(-06)	4.23(-06)	4.31(-06)
Ca	2.24(-03)	3.41(-03)	3.99(-03)	4.19(-03)	4.23(-03)
Sc	2.14(-08)	2.29(-08)	2.38(-08)	1.69(-06)	7.92(-06)
Ti	5.85(-06)	2.37(-05)	3.72(-05)	9.09(-05)	1.42(-04)
V	2.19(-07)	6.16(-07)	7.72(-07)	7.97(-07)	7.97(-07)
Cr	6.06(-05)	3.16(-04)	5.60(-04)	7.82(-04)	8.53(-04)
Mn	1.24(-05)	3.34(-05)	4.40(-05)	4.68(-05)	4.68(-05)
Fe	1.12(-03)	5.21(-03)	1.03(-02)	5.08(-02)	6.64(-02)
Co	2.13(-08)	2.21(-08)	2.25(-08)	1.92(-04)	3.77(-04)
Ni	1.84(-05)	3.53(-05)	4.60(-05)	8.44(-04)	1.53(-03)
Cu	1.23(-14)	1.23(-14)	1.23(-14)	3.59(-14)	3.22(-13)
Zn	5.76(-14)	5.76(-14)	5.76(-14)	1.22(-08)	4.62(-08)

TABLE A6
EXPLOSIVE NUCLEOSYNTHESIS OF THE $20 M_{\odot}$ $Z = 2 \cdot 10^{-2}$ MODEL

	(1)	(2)	(3)	(4)	(5)	(6)	(7)	(8)
M(^{56}Ni)	0.001	0.005	0.010	0.050	0.100	0.150	0.200	0.244
M _{ejected}	17.76	17.81	17.84	17.90	17.96	18.02	18.09	18.16
M _{cut}	2.24	2.19	2.16	2.10	2.04	1.98	1.91	1.84
C	3.05(-01)	3.05(-01)	3.05(-01)	3.05(-01)	3.05(-01)	3.05(-01)	3.05(-01)	3.05(-01)
N	7.31(-02)	7.31(-02)	7.31(-02)	7.31(-02)	7.31(-02)	7.31(-02)	7.31(-02)	7.31(-02)
O	1.19(+00)	1.19(+00)	1.19(+00)	1.19(+00)	1.19(+00)	1.19(+00)	1.19(+00)	1.19(+00)
F	6.82(-06)	6.82(-06)	6.82(-06)	6.82(-06)	6.82(-06)	6.82(-06)	6.82(-06)	6.82(-06)
Ne	9.42(-02)	9.42(-02)	9.42(-02)	9.42(-02)	9.42(-02)	9.42(-02)	9.42(-02)	9.42(-02)
Na	2.59(-03)	2.59(-03)	2.59(-03)	2.59(-03)	2.59(-03)	2.59(-03)	2.59(-03)	2.59(-03)
Mg	4.30(-02)	4.30(-02)	4.30(-02)	4.30(-02)	4.30(-02)	4.30(-02)	4.30(-02)	4.30(-02)
Al	2.95(-03)	2.95(-03)	2.95(-03)	2.95(-03)	2.95(-03)	2.95(-03)	2.95(-03)	2.95(-03)
Si	1.67(-01)	1.92(-01)	2.03(-01)	2.10(-01)	2.10(-01)	2.10(-01)	2.10(-01)	2.10(-01)
P	1.35(-03)	1.35(-03)	1.35(-03)	1.35(-03)	1.35(-03)	1.35(-03)	1.35(-03)	1.35(-03)
S	8.76(-02)	1.02(-01)	1.10(-01)	1.17(-01)	1.17(-01)	1.17(-01)	1.17(-01)	1.17(-01)
Cl	3.91(-04)	3.91(-04)	3.91(-04)	3.91(-04)	3.91(-04)	3.91(-04)	3.92(-04)	3.92(-04)
Ar	1.47(-02)	1.72(-02)	1.88(-02)	2.07(-02)	2.07(-02)	2.07(-02)	2.07(-02)	2.07(-02)
K	2.32(-04)	2.32(-04)	2.32(-04)	2.32(-04)	2.32(-04)	2.33(-04)	2.33(-04)	2.33(-04)
Ca	7.56(-03)	9.64(-03)	1.11(-02)	1.36(-02)	1.36(-02)	1.37(-02)	1.37(-02)	1.38(-02)
Sc	2.10(-06)	2.11(-06)	2.11(-06)	2.12(-06)	2.12(-06)	2.12(-06)	2.14(-06)	2.15(-06)
Ti	1.01(-04)	1.24(-04)	1.47(-04)	2.18(-04)	2.38(-04)	2.78(-04)	3.42(-04)	4.02(-04)
V	1.61(-05)	2.06(-05)	2.34(-05)	2.98(-05)	2.98(-05)	2.98(-05)	2.98(-05)	2.98(-05)
Cr	6.08(-04)	9.64(-04)	1.32(-03)	2.83(-03)	2.86(-03)	2.92(-03)	3.00(-03)	3.09(-03)
Mn	4.34(-04)	5.98(-04)	7.27(-04)	1.15(-03)	1.15(-03)	1.15(-03)	1.15(-03)	1.15(-03)
Fe	2.96(-02)	3.61(-02)	4.24(-02)	8.54(-02)	1.37(-01)	1.89(-01)	2.41(-01)	2.88(-01)
Co	2.25(-04)	2.25(-04)	2.25(-04)	2.52(-04)	5.03(-04)	8.60(-04)	1.50(-03)	2.29(-03)
Ni	2.47(-03)	2.63(-03)	2.73(-03)	3.36(-03)	5.91(-03)	8.53(-03)	1.07(-02)	1.21(-02)
Cu	1.32(-04)	1.32(-04)	1.32(-04)	1.32(-04)	1.32(-04)	1.32(-04)	1.32(-04)	1.32(-04)
Zn	2.34(-04)	2.34(-04)	2.34(-04)	2.34(-04)	2.34(-04)	2.34(-04)	2.35(-04)	2.35(-04)

TABLE A7
EXPLOSIVE NUCLEOSYNTHESIS OF THE $20 M_{\odot}$ $Z = 10^{-3}$ MODEL

	(1)	(2)	(3)	(4)	(5)	(6)	(7)	(8)
M(^{56}Ni)	0.001	0.005	0.010	0.050	0.100	0.150	0.200	0.225
M _{ejected}	18.07	18.12	18.14	18.21	18.27	18.33	18.40	18.44
M _{cut}	1.93	1.88	1.86	1.79	1.73	1.67	1.60	1.56
C	2.75(-01)	2.75(-01)	2.75(-01)	2.75(-01)	2.75(-01)	2.75(-01)	2.75(-01)	2.75(-01)
N	4.76(-03)	4.76(-03)	4.76(-03)	4.76(-03)	4.76(-03)	4.76(-03)	4.76(-03)	4.76(-03)
O	1.02(+00)	1.02(+00)	1.02(+00)	1.02(+00)	1.02(+00)	1.02(+00)	1.02(+00)	1.02(+00)
F	4.16(-07)	4.16(-07)	4.16(-07)	4.16(-07)	4.16(-07)	4.16(-07)	4.16(-07)	4.16(-07)
Ne	2.00(-01)	2.00(-01)	2.00(-01)	2.00(-01)	2.00(-01)	2.00(-01)	2.00(-01)	2.00(-01)
Na	2.02(-03)	2.02(-03)	2.02(-03)	2.02(-03)	2.02(-03)	2.02(-03)	2.02(-03)	2.02(-03)
Mg	7.42(-02)	7.42(-02)	7.42(-02)	7.42(-02)	7.42(-02)	7.42(-02)	7.42(-02)	7.42(-02)
Al	1.28(-03)	1.28(-03)	1.28(-03)	1.28(-03)	1.28(-03)	1.28(-03)	1.28(-03)	1.28(-03)
Si	8.00(-02)	1.02(-01)	1.13(-01)	1.21(-01)	1.21(-01)	1.21(-01)	1.21(-01)	1.21(-01)
P	1.64(-04)	1.64(-04)	1.64(-04)	1.64(-04)	1.64(-04)	1.64(-04)	1.64(-04)	1.64(-04)
S	3.69(-02)	5.05(-02)	5.83(-02)	6.60(-02)	6.60(-02)	6.60(-02)	6.60(-02)	6.60(-02)
Cl	5.81(-05)	5.82(-05)	5.82(-05)	5.82(-05)	5.83(-05)	5.83(-05)	5.85(-05)	5.85(-05)
Ar	5.90(-03)	8.33(-03)	9.89(-03)	1.20(-02)	1.20(-02)	1.20(-02)	1.20(-02)	1.20(-02)
K	2.37(-05)	2.37(-05)	2.37(-05)	2.37(-05)	2.38(-05)	2.40(-05)	2.42(-05)	2.44(-05)
Ca	4.45(-03)	6.47(-03)	7.96(-03)	1.06(-02)	1.06(-02)	1.07(-02)	1.07(-02)	1.08(-02)
Sc	1.27(-07)	1.30(-07)	1.32(-07)	1.36(-07)	1.42(-07)	1.42(-07)	1.76(-07)	1.84(-07)
Ti	1.05(-05)	3.30(-05)	5.58(-05)	1.23(-04)	1.49(-04)	1.93(-04)	2.69(-04)	2.98(-04)
V	9.51(-07)	2.13(-06)	3.02(-06)	4.81(-06)	4.81(-06)	4.81(-06)	4.82(-06)	4.82(-06)
Cr	8.75(-05)	3.81(-04)	7.11(-04)	2.05(-03)	2.09(-03)	2.15(-03)	2.25(-03)	2.29(-03)
Mn	3.89(-05)	9.04(-05)	1.33(-04)	2.63(-04)	2.63(-04)	2.63(-04)	2.63(-04)	2.63(-04)
Fe	2.59(-03)	6.94(-03)	1.22(-02)	5.29(-02)	1.04(-01)	1.56(-01)	2.08(-01)	2.36(-01)
Co	1.44(-05)	1.44(-05)	1.44(-05)	5.25(-05)	2.92(-04)	6.81(-04)	1.52(-03)	2.06(-03)
Ni	1.28(-04)	1.57(-04)	1.77(-04)	2.57(-04)	7.31(-04)	2.65(-03)	4.30(-03)	5.59(-03)
Cu	3.01(-06)	3.01(-06)	3.01(-06)	3.01(-06)	3.01(-06)	3.01(-06)	3.01(-06)	3.01(-06)
Zn	6.18(-06)	6.18(-06)	6.18(-06)	6.18(-06)	6.19(-06)	6.23(-06)	6.31(-06)	6.49(-06)

TABLE A8
EXPLOSIVE NUCLEOSYNTHESIS OF THE $20 M_{\odot}$ $Z = 0$ MODEL

	(1)	(2)	(3)	(4)	(5)	(6)	(7)
$M(^{56}\text{Ni})$	0.001	0.005	0.010	0.050	0.100	0.150	0.201
M_{ejected}	18.02	18.07	18.10	18.16	18.22	18.29	18.36
M_{cut}	1.98	1.93	1.90	1.84	1.78	1.71	1.64
C	2.48(-01)	2.48(-01)	2.48(-01)	2.48(-01)	2.48(-01)	2.48(-01)	2.48(-01)
N	4.24(-03)	4.24(-03)	4.24(-03)	4.24(-03)	4.24(-03)	4.24(-03)	4.24(-03)
O	9.15(-01)	9.15(-01)	9.15(-01)	9.15(-01)	9.15(-01)	9.15(-01)	9.15(-01)
F	3.01(-10)	3.01(-10)	3.01(-10)	3.01(-10)	3.01(-10)	3.01(-10)	3.01(-10)
Ne	1.05(-01)	1.05(-01)	1.05(-01)	1.05(-01)	1.05(-01)	1.05(-01)	1.05(-01)
Na	5.37(-04)	5.37(-04)	5.37(-04)	5.37(-04)	5.37(-04)	5.37(-04)	5.37(-04)
Mg	6.05(-02)	6.05(-02)	6.05(-02)	6.05(-02)	6.05(-02)	6.05(-02)	6.05(-02)
Al	4.67(-04)	4.67(-04)	4.67(-04)	4.67(-04)	4.67(-04)	4.67(-04)	4.67(-04)
Si	8.42(-02)	1.07(-01)	1.21(-01)	1.31(-01)	1.31(-01)	1.31(-01)	1.31(-01)
P	7.80(-05)	7.83(-05)	7.86(-05)	7.92(-05)	7.93(-05)	7.93(-05)	7.94(-05)
S	4.16(-02)	5.64(-02)	6.57(-02)	7.45(-02)	7.45(-02)	7.45(-02)	7.45(-02)
Cl	3.46(-05)	3.47(-05)	3.47(-05)	3.48(-05)	3.50(-05)	3.52(-05)	4.36(-05)
Ar	6.93(-03)	9.60(-03)	1.14(-02)	1.37(-02)	1.37(-02)	1.37(-02)	1.37(-02)
K	1.39(-05)	1.40(-05)	1.40(-05)	1.40(-05)	1.40(-05)	1.40(-05)	1.41(-05)
Ca	5.78(-03)	8.06(-03)	9.73(-03)	1.25(-02)	1.25(-02)	1.26(-02)	1.27(-02)
Sc	6.35(-08)	6.61(-08)	6.79(-08)	7.21(-08)	1.66(-07)	2.77(-07)	7.89(-06)
Ti	8.80(-06)	3.14(-05)	5.56(-05)	1.24(-04)	1.54(-04)	2.08(-04)	2.89(-04)
V	3.50(-07)	9.98(-07)	1.51(-06)	2.36(-06)	2.36(-06)	2.36(-06)	2.36(-06)
Cr	6.46(-05)	3.48(-04)	6.84(-04)	2.06(-03)	2.10(-03)	2.17(-03)	2.29(-03)
Mn	1.77(-05)	4.79(-05)	7.31(-05)	1.35(-04)	1.35(-04)	1.35(-04)	1.35(-04)
Fe	1.23(-03)	5.38(-03)	1.05(-02)	5.08(-02)	1.02(-01)	1.53(-01)	2.05(-01)
Co	5.15(-08)	5.25(-08)	5.31(-08)	7.77(-06)	1.75(-04)	6.42(-04)	9.46(-04)
Ni	2.77(-05)	4.44(-05)	5.72(-05)	1.70(-04)	6.72(-04)	9.70(-04)	2.39(-03)
Cu	6.30(-14)	6.30(-14)	6.30(-14)	6.30(-14)	6.77(-14)	9.89(-14)	1.73(-13)
Zn	1.93(-13)	1.93(-13)	1.93(-13)	3.45(-11)	4.95(-09)	2.05(-08)	4.84(-08)

TABLE A9
EXPLOSIVE NUCLEOSYNTHESIS OF THE $25 M_{\odot}$ $Z = 2 \cdot 10^{-2}$ MODEL

TABLE A10
EXPLOSIVE NUCLEOSYNTHESIS OF THE $25 M_{\odot}$ $Z = 10^{-3}$ MODEL

TABLE A11
EXPLOSIVE NUCLEOSYNTHESIS OF THE $25 M_{\odot}$ $Z = 0$ MODEL

	(1)	(2)	(3)	(4)	(5)	(6)	(7)	(8)
$M(^{56}\text{Ni})$	0.001	0.005	0.010	0.050	0.100	0.150	0.200	0.413
M_{ejected}	22.37	22.43	22.48	22.59	22.64	22.70	22.75	23.01
M_{cut}	2.63	2.57	2.52	2.41	2.36	2.30	2.25	1.99
C	4.71(-01)	4.71(-01)	4.71(-01)	4.71(-01)	4.71(-01)	4.71(-01)	4.71(-01)	4.71(-01)
N	3.03(-03)	3.03(-03)	3.03(-03)	3.03(-03)	3.03(-03)	3.03(-03)	3.03(-03)	3.03(-03)
O	2.13(+00)	2.13(+00)	2.13(+00)	2.13(+00)	2.13(+00)	2.13(+00)	2.13(+00)	2.13(+00)
F	1.88(-10)	1.88(-10)	1.88(-10)	1.88(-10)	1.88(-10)	1.88(-10)	1.88(-10)	1.88(-10)
Ne	2.58(-01)	2.58(-01)	2.58(-01)	2.58(-01)	2.58(-01)	2.58(-01)	2.58(-01)	2.58(-01)
Na	2.60(-04)	2.60(-04)	2.60(-04)	2.60(-04)	2.60(-04)	2.60(-04)	2.60(-04)	2.60(-04)
Mg	1.09(-01)	1.09(-01)	1.09(-01)	1.09(-01)	1.09(-01)	1.09(-01)	1.09(-01)	1.09(-01)
Al	4.31(-04)	4.31(-04)	4.31(-04)	4.31(-04)	4.31(-04)	4.31(-04)	4.31(-04)	4.31(-04)
Si	1.39(-01)	1.70(-01)	1.94(-01)	2.24(-01)	2.24(-01)	2.24(-01)	2.24(-01)	2.24(-01)
P	7.78(-05)	7.83(-05)	7.88(-05)	8.05(-05)	8.06(-05)	8.06(-05)	8.07(-05)	8.09(-05)
S	7.34(-02)	9.33(-02)	1.08(-01)	1.32(-01)	1.32(-01)	1.32(-01)	1.32(-01)	1.32(-01)
Cl	5.04(-05)	5.05(-05)	5.05(-05)	5.06(-05)	5.07(-05)	5.11(-05)	5.17(-05)	6.63(-05)
Ar	1.26(-02)	1.63(-02)	1.90(-02)	2.44(-02)	2.47(-02)	2.47(-02)	2.47(-02)	2.48(-02)
K	2.18(-05)	2.18(-05)	2.18(-05)	2.19(-05)	2.19(-05)	2.19(-05)	2.19(-05)	2.21(-05)
Ca	1.07(-02)	1.41(-02)	1.64(-02)	2.24(-02)	2.30(-02)	2.30(-02)	2.30(-02)	2.32(-02)
Sc	1.42(-07)	1.46(-07)	1.48(-07)	1.55(-07)	1.74(-07)	3.53(-07)	6.53(-07)	1.50(-05)
Ti	1.25(-05)	3.73(-05)	6.52(-05)	1.92(-04)	2.22(-04)	2.48(-04)	2.78(-04)	4.59(-04)
V	3.40(-07)	9.05(-07)	1.51(-06)	3.00(-06)	3.21(-06)	3.21(-06)	3.21(-06)	3.21(-06)
Cr	6.77(-05)	3.50(-04)	7.14(-04)	2.91(-03)	3.72(-03)	3.75(-03)	3.80(-03)	4.05(-03)
Mn	1.76(-05)	4.55(-05)	7.46(-05)	1.64(-04)	1.87(-04)	1.87(-04)	1.87(-04)	1.87(-04)
Fe	1.24(-03)	5.37(-03)	1.05(-02)	5.08(-02)	1.01(-01)	1.52(-01)	2.02(-01)	4.18(-01)
Co	1.37(-07)	1.38(-07)	1.38(-07)	1.39(-07)	2.15(-05)	7.05(-05)	1.25(-04)	5.37(-04)
Ni	3.81(-05)	5.46(-05)	6.89(-05)	1.10(-04)	3.64(-04)	1.13(-03)	1.93(-03)	6.58(-03)
Cu	3.27(-13)	3.27(-13)	3.27(-13)	3.27(-13)	3.27(-13)	3.28(-13)	3.29(-13)	3.60(-13)
Zn	1.08(-12)	1.08(-12)	1.08(-12)	1.08(-12)	2.19(-10)	2.19(-09)	5.15(-09)	3.71(-08)